

Drug resistance revealed by in silico deep mutational scanning and mutation tracker

Dong Chen¹, Gengzhuo Liu¹, Hongyan Du¹, Junjie Wee¹, Rui Wang², Jiahui Chen³, Jana Shen⁴, and Guo-Wei Wei^{†1,5,6}

¹*Department of Mathematics, Michigan State University, MI, 48824, USA*

²*Simons Center for Computational Physical Chemistry, New York University, New York, NY, 10003*

³*Department of Mathematical Sciences, University of Arkansas, Fayetteville, AR 72701*

⁴*Department of Pharmaceutical Sciences, University of Maryland School of Pharmacy, Baltimore, MD 21201*

⁵*Department of Electrical and Computer Engineering, Michigan State University, MI 48824, USA*

⁶*Department of Biochemistry and Molecular Biology, Michigan State University, MI 48824, USA*

Abstract As COVID-19 enters its fifth year, it continues to pose a significant global health threat, with the constantly mutating SARS-CoV-2 virus challenging drug effectiveness. A comprehensive understanding of virus-drug interactions is essential for predicting and improving drug effectiveness, especially in combating drug resistance during the pandemic. In response, the Path Laplacian Transformer-based Prospective Analysis Framework (PLFormer-PAF) has been proposed, integrating historical data analysis and predictive modeling strategies. This dual-strategy approach utilizes path topology to transform protein-ligand complexes into topological sequences, enabling the use of advanced large language models for analyzing protein-ligand interactions and enhancing its reliability with factual insights garnered from historical data. It has shown unparalleled performance in predicting binding affinity tasks across various benchmarks, including specific evaluations related to SARS-CoV-2, and assesses the impact of virus mutations on drug efficacy, offering crucial insights into potential drug resistance. The predictions align with observed mutation patterns in SARS-CoV-2, indicating that the widespread use of the Pfizer drug has led to viral evolution and reduced drug efficacy. PLFormer-PAF’s capabilities extend beyond identifying drug-resistant strains, positioning it as a key tool in drug discovery research and the development of new therapeutic strategies against fast-mutating viruses like COVID-19.

Keywords Drug resistance, Virus Mutation, Path Topology, Multiscale Topology, Path Laplacian.

[†]Corresponding author: weig@msu.edu

Contents

1	Introduction	3
2	Results	4
2.1	Overview of PLFormer-based drug resistance revelation framework	4
2.2	Prediction of viral mutations and drug resistance.	6
2.3	Evaluating PLFormer on PDBbind benchmarks.	11
2.4	Evaluating PLFormer on SARS-CoV(-2) BA dataset.	13
3	Discussion	15
4	Methods	17
4.1	Datasets	17
4.2	Path topological sequence embedding	18
4.3	PLFormer model	25
A	Supplementary Information	28
A.1	Evaluation metrics	28
A.2	Hyperparameter selection and optimization	28
A.3	Topological objects	30
A.4	Vietoris-Rips path complex and alpha path complex	32
A.5	Element-specific topology	35
A.6	PLFormer components	36
A.7	Supplementary tables	38
A.8	Supplementary figures	41

1 Introduction

Currently in its fifth year, society has adapted to the persistent presence of COVID-19, which has stabilized as an endemic situation. Despite this stability, SARS-CoV-2 continues to cause thousands of deaths monthly. The virus’s continuous evolution raises concerns about resistance to existing treatments [1], especially given the reliance on Pfizer’s PAXLOVID [2, 3], the primary FDA-approved therapy targeting the viral main protease [4]. To combat these issues, it is crucial to deeply understand how the virus interacts with therapeutic drugs, with a focus on protein-ligand interactions. These interactions, pivotal in drug efficacy, involve drug molecules binding to enzymes or receptors, affecting biological functions and managing various health conditions [5]. The evolving nature of the virus can lead to alterations in protein structures, impacting these critical binding affinities [6]. In pharmacology and medicinal chemistry, comprehending these binding dynamics is essential for the effectiveness and specificity of treatments. The ongoing COVID-19 situation has highlighted this, particularly as mutations in the virus’s main protease alter drug binding affinities, impacting the effectiveness of antiviral therapies [7]. On the other hand, the COVID-19 pandemic’s historical progress has offered valuable opportunities to examine virus mutation patterns, providing crucial insights into the evolution of SARS-CoV-2. By utilizing data from the Global Initiative on Sharing All Influenza Data (GISAID) [8] and employing advanced sequencing and genotyping methods [9], a detailed dataset of viral mutations has been compiled. This information is vital for analyzing evolutionary trends and drug resistance challenges.

The introduction of ‘deep mutational scanning’ (DMS) has revolutionized computational biology by producing extensive datasets that shed light on the fundamental properties of proteins, essential for understanding the nature of mutations [10]. These datasets include resources like the Binding Database (BindingDB) [11], the Protein Data Bank (PDB) [12], and PDBbind [13]. When combined with the rich information in biochemical databases, these resources offer a unique opportunity to model and assess the impact of protein mutations on drug binding. However, there are still challenges in this area, particularly for deep learning-based computational methods. These methods often face difficulties in obtaining labeled data for protein-ligand complexes, and there are significant concerns about the accuracy and generalizability of these models in predicting binding affinity changes due to mutations in drug targets.

On the other hand, the success of the Transformer framework and models such as ChatGPT, which utilize extensive pre-training and strategic use of unlabeled data, highlights the potential of self-supervised learning in situations where traditional labeled data are scarce or inadequate [14, 15]. These models suggest new ways to address some limitations of current computational methods in drug discovery [16, 17]. However, applying these advanced techniques directly to drug discovery, particularly in modeling protein-ligand complexes, presents unique challenges. One significant issue is the potential overlook of critical stereochemical relationships, which are crucial in accurately modeling and predicting protein-ligand interactions. This gap calls for tailored approaches that can effectively incorporate the three-dimensional (3D) complex nature of these interactions, ensuring that the predictive models are not only powerful and data-efficient but also chemically and biologically accurate.

To combat these critical challenges in the ongoing fight against COVID-19, this study introduces a new topological deep learning (TDL) method called Path Laplacian Transformer-based Prospective Analysis Framework (PLFormer-PAF), a two-pronged strategy framework. The first

component, termed the Historical Data Analysis Strategy and elaborated in Figure 1a, leverages an extensive collection of medical test outcomes and authentic historical records, referred to as the mutation tracker, to analyze mutation trends. PLFormer-PAF, by examining extensive datasets from biochemical and medical sources, provides an in-depth understanding of past protein interactions with drugs or vaccines. This analysis is key for grasping the inherent characteristics of proteins and drugs, vital for predicting future interactions. The second component is the Predictive Modeling Strategy, also shown in 1b. This strategy centers around the Path Laplacian Transformer (PLFormer), employing advanced natural language processing (NLP) models for prospective analysis. Essentially, PLFormer grounded in persistent path Laplacian (PPL)[18] and element-specific multiscale technique [19] to convert 3D spatial protein-ligand (drug) information into a 1D sequential representation suitable for NLP modeling. By translating complex 3D structures into topological sequences, the PLFormer adapts the sequential architecture of Transformers for analyzing protein-ligand complexes, marking a significant paradigm shift in understanding the biological complex interactions. This model has shown state-of-the-art performance across various benchmark datasets focused on protein-ligand binding affinity prediction. It also demonstrated remarkable efficacy in predicting the impact of SARS-CoV-2 mutations on drug binding. This contributes valuable perspectives on deep mutational scanning (DMS) and potential mechanisms of drug resistance, thereby facilitating the advancement of future drug development efforts.

The synergy of these strategies forms the core strength of PLFormer-PAF. The historical data analysis provides a solid base for constructing accurate predictive models, while also serving as a validation tool for these models. This bidirectional flow of information fosters a framework that is continuously evolving and self-improving. By validating predictive outcomes with historical facts, PLFormer-PAF enhances its reliability and accuracy, making it an indispensable tool in the fields of pharmacology, medicinal chemistry, and drug development. As the battle against diseases like COVID-19 and seasonal flu continues, PLFormer-PAF’s insights are instrumental in addressing the drug resistance problem, ensuring our strategies remain adaptive to the changing nature of viral pathogens.

2 Results

In this section, we first provide an overview of PLFormer-PAF. Following this introduction, we demonstrate PLFormer-PAF’s versatility in the accurate prediction of the evolution of SARS-CoV-2 and the drug resistance of PAXLOVID, showcasing its applicability in specialized and crucial areas of viral evolution and pharmacological resistance. Additionally, the key component PLFormer model is thoroughly evaluated via several critical tasks. These include binding affinity prediction on CASF-2007, CASF-2013, and CASF-2016 benchmarks, and a 5-fold cross-validation analysis using the SARS-CoV(-2) binding affinity (BA) dataset.

2.1 Overview of PLFormer-based drug resistance revelation framework

Figure 1a presents a comprehensive process of historical data analysis strategy. This process initiates with testing for the virus in patients during an outbreak. As of November 29, 2023, a total of 3,694,942 samples have been collected. Utilizing this real-world data, the Global Initiative on Sharing All Influenza Data (GISAID) plays a pivotal role in analyzing and tracking viral variants

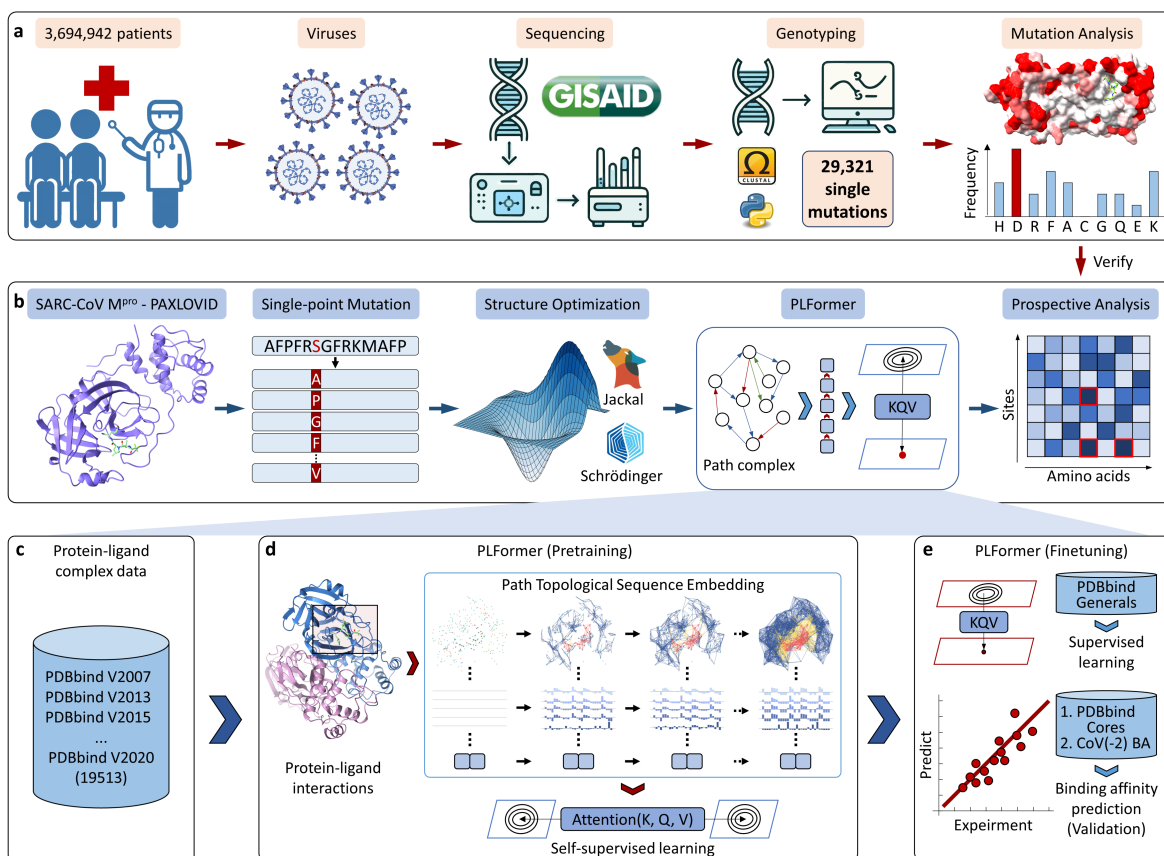


Figure 1: Schematic illustration of Path Laplacian Transformer-based Prospective Analysis Framework. **a**, Illustration of the extensive process involved in historical data analysis strategy of the prevalent SARS-CoV-2 virus. It encompasses a series of steps including testing for the virus, sequencing the viral genome, conducting genotyping, and analyzing the frequency of mutations. **b**, Demonstration of a predictive modeling strategy on the mutations of SARS-CoV-2 M^{Pro} and the resulting drug resistance issues with Pfizer’s drug PAXLOVID. **c-e**, Workflow of the proposed PLFormer model: A dataset of label-free protein-ligand complexes was compiled (**c**). This dataset was employed to pretrain the PLFormer (**d**). Subsequently, the PLFormer was fine-tuned using a dataset of labeled protein-ligand complexes and its performance was assessed through various binding affinity prediction tasks (**e**).

across the globe. In response to the COVID-19 pandemic, GISAID notably expanded its scope to include the sharing of genomic data of the SARS-CoV-2 virus, thereby becoming instrumental in monitoring the emergence and spread of various SARS-CoV-2 variants worldwide. Particularly, a key technique employed in our study is single nucleotide polymorphism (SNP) genotyping, which is essential for studying the genetic diversity within the SARS-CoV-2 species and for monitoring genotypic changes as the virus transmits and evolves. Employing multiple sequence alignment techniques, we aligned genome sequences with the reference SARS-CoV-2 genome, resulting in 3,694,942 SNP profiles from all the complete genomes collected by the specified date. After removing duplicate mutation types, we identified 29,321 unique single mutations. Each of these SNP profiles represents a unique deviation from the standard reference genome sequence, effectively documenting the unique genotype of each individual SARS-CoV-2 variant. Our research focused primarily on the SNP profiles of the SARS-CoV-2 main protease (M^{Pro}). The findings from this analysis of single mutations are invaluable for future research, particularly in understanding and predicting patterns,

trends, and even drug resistance of Pfizer drug PAXLOVID in subsequent mutations of the virus.

To conduct a prospective analysis on the mutations of SARS-CoV-2 M^{Pro} and the resulting drug resistance with Pfizer’s drug PAXLOVID, we introduced a silico deep mutational scanning strategy within the PLFormer-PAF as shown in Figure 1b. The structural basis of this analysis is the SARS-CoV-2 M^{Pro} and PAXLOVID complex (PDB ID 7VH8). To grasp the implications of mutations, in silico deep mutational scanning is employed to explore all possible mutations. Specifically, systematic single-point mutations are introduced at 21 critical residues for protein-ligand interactions, resulting in a comprehensive analysis of 19×21 mutations. For each mutation, a structure optimization process is employed to avoid unrealistic atomic positions and ensure the reliability of the complex structure. Crucially, the PLFormer model is utilized to predict the binding affinities of all the protein-ligand complexes, including both the mutated and original structures. This approach allows for an in-depth analysis of the affinity changes caused by these mutations. The variation in binding affinity is then used to analyze the drug resistance of PAXLOVID, predicting the likelihood of mutations that could lead to resistance. The results of this analysis are corroborated by historical data analysis as shown in Figure 1a. The observed changes in mutation frequency, particularly following the use of PAXLOVID, are indicative of viral escape mechanisms and the potential for drug resistance. This highlights the dynamic nature of viral evolution in response to pharmacological interventions. The methodology and process outlined offer significant insights and serve as a valuable reference for clinical medication strategies, particularly in the context of managing drug resistance in evolving viral pathogens like SARS-CoV-2.

Essentially, the proposed PLFormer is a groundbreaking strategy in the computational analysis of protein-ligand complexes, detailed in Figure 1 c-e, comprising three key phases. Initially, it compiles a vast, unlabeled database of protein-ligand complexes from PDBbind versions v2007 to v2020, amassing 19,513 unique complexes. The second stage, illustrated in Figure 1d, involves training the PLFormer using a self-supervised learning approach on this extensive dataset. The model’s effectiveness is then carefully evaluated; the pre-trained PLFormer is fine-tuned using labeled data from the PDBbind v2020 dataset. This enhanced model is subsequently used for predicting protein-ligand binding affinities across three benchmark datasets (i.e., CASF-2007, CASF-2013, and CASF-2016) and is applied to specialized SARS-CoV and SARS-CoV-2 datasets, employing a 5-fold cross-validation method as shown in Figure 1e. Crucially, PLFormer’s generalization capabilities extend to analyzing drug resistance driven by viral mutations, providing precise predictions in mutation analysis and drug resistance. This model not only sheds light on the complexities of protein-ligand interactions but also studies the vital area of assessing the effects of viral mutations on drug resistance, offering substantial contributions to the molecular mechanism of drug resistance. For an in-depth understanding of PLFormer, refer to the Method section 4. And a summary of the data used is listed in Table 3.

2.2 Prediction of viral mutations and drug resistance.

In this section, we commence our analysis by examining the structure of SARS-CoV-2 main protease (M^{Pro}) in conjunction with the FDA-approved drug, PAXLOVID. Our focus then shifts to assessing the relative mutation frequency of SARS-CoV-2 M^{Pro}, comparing periods before and after the widespread application of PAXLOVID. This analysis aims to elucidate the impact of PAXLOVID’s usage on the evolution of the virus, particularly in terms of drug resistance devel-

opment. Following this, we simulate single-point mutations in the SARS-CoV-2 M^{pro} near the drug-binding site. The goal here is to predict and analyze the potential implications of these mutations on PAXLOVID resistance. Through this comprehensive approach, we seek to better understand the dynamics of viral evolution in the context of drug exposure and its consequent effects on therapeutic efficacy.

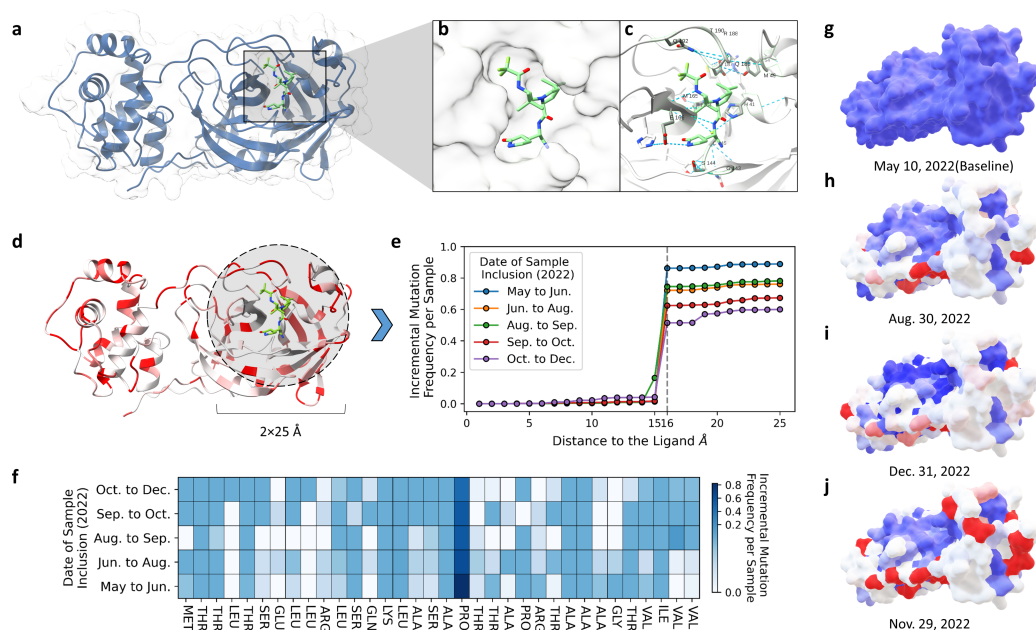


Figure 2: The structure of SARS-CoV-2 M_{pro} in complex with the drug PAXLOVID. **a**, Overview of the SARS-CoV-2 M_{pro} structure. The binding pocket for the ligand is highlighted within a black box. PAXLOVID is shown as a stick model with carbon atoms in bright green, oxygen atoms in bright red, and nitrogen atoms in blue. **b**, The close-up view of the substrate-binding pocket. **c**, Detailed binding model of the SARS-CoV-2 M_{pro} -PAXLOVID complex. Key residues involved in inhibitor binding are labeled, and the interactions are depicted with cyan dashed lines. **d**, Ribbon style of mutation frequency in SARS-CoV-2 M_{pro} . It shows the frequency of mutations in each residue of the SARS-CoV-2 M_{pro} . The intensity of red coloration corresponds to the mutation frequency. A black circle indicates the area within a 25 Å radius around PAXLOVID. **e**, Incremental mutation frequency in SARS-CoV-2 M_{pro} relative to the radius around PAXLOVID. It displays the variation in mutation frequency in the SARS-CoV-2 M_{pro} as a function of the radial distance from PAXLOVID. **f**, The incremental mutation frequency per sample within a 16 Å radius around PAXLOVID. The color intensity of the box represents the strength of the incremental mutation frequency. **g-j**, Incremental mutation frequency in SARS-CoV-2 M_{pro} 3D models across various dates, with frequencies calculated relative to the baseline date of 05/10/2022. This color-coded visualization represents the protein surface, where white denotes areas with low mutation frequencies (under 10). A gradient from blue to white indicates moderate frequencies (ranging from 10 to 50). A gradient from white to red indicates frequencies (ranging from 50 to 100). Areas with incremental frequencies exceeding 100 are highlighted in red. The incremental mutation frequency is displayed for the following dates: **g** baseline up to 05/10/2022; **h** up to 08/30/2022; **i** up to 12/31/2022; and **j** up to 11/29/2023.

Figure 2a presents the crystal structure of the complex, including SARS-CoV-2 M^{pro} and the FDA-approved drug, PAXLOVID (PDB ID 7VH8). A detailed view is provided in Figure 2b, which zooms in on the drug's pose within the M^{pro} 's binding pocket. This is critical for appreciating the drug's precise molecular alignment. Furthermore, Figure 2c reveals the detailed binding model, showcasing the residues participating in the inhibition process, thereby offering a 3D perspective of

the protein-ligand interactions. Specifically, building on this structural foundation, we focus on 21 key residues surrounding the drug binding site on SARS-CoV-2 M^{Pro}, as identified[20], including Q192, T190, Q189, E166, R188, D187, Y54, M49, H164, M165, H41, C145, G143, S144, N142, L141, F140, H172, H163, E166, L167, P168. These residues are instrumental in predicting and analyzing the drug’s impact on the virus.

In genetics and bioinformatics, a single nucleotide polymorphism (SNP) is a one-letter substitution where a single nucleotide at a specific position in the genome varies from another in the genome sequence [9]. To study the genetic diversity within a species, the technique of SNP genotyping is employed, particularly to monitor the genotypic alterations as SARS-CoV-2 transmits and evolves[21, 22]. Through the use of multiple sequence alignment techniques to reorganize genome sequences in alignment with the reference SARS-CoV-2 genome, we have obtained 3,694,942 SNP profiles for all the complete SARS-CoV-2 genomes collected on November 29, 2023. Each SNP profile, linked to a specific SARS-CoV-2 genome, documents every deviation from a standard reference genome sequence, thus representing the unique genotype of that individual SARS-CoV-2 variant. The Figure 13 presents an up-to-date mutation tracker for SARS-CoV-2 as of November 29, 2023. In this work, we mainly studied the SNP profiles of SARS-CoV-2 main protease (M^{Pro}), as shown in Figure 2a. Our study extends to examining the mutation frequency of this main protease around the United States. As depicted in Figure 2d, we demonstrated the latest (up to December 2023) mutation frequency distributions on the SARS-CoV-2 M^{Pro}, with the intensity of red indicating mutation frequency. In the supplementary material, we have included detailed information on the mutation frequency and the progression of these mutations over time in SARS-CoV-2 M^{Pro}. This is illustrated through 3D rotatable models corresponding to key dates: 05/10/2022, prior to the widespread use of the drug; 08/30/2022, marking the period of the drug’s most extensive usage; 12/31/2022, after the drug’s peak usage; and 11/29/2023, representing the most recent data available for this study. These models are instrumental in depicting the evolutionary trajectory of the virus and how the mutation frequency in SARS-CoV-2 M^{Pro} has been influenced by the application of the drug. This visualization aids in understanding the dynamic nature of the virus under pharmacological pressure. The stationary illustration of mutation frequencies, depicted in a ribbon style, is presented in Figure 14. Meanwhile, the illustration of incremental mutation frequencies is available in Figure 2g-j.

An intriguing aspect of our analysis on the domain with a 25 Å radius from PAXLOVID is shown as black area in Figure 2d. It is illustrated in Figure 2e, which displays the incremental mutation frequency per sample (relative mutation frequency) over different time periods. This figure reveals a stable relative mutation rate within a 0 to 15 Å radius from the ligand, indicating the resilience of the binding site. However, a marked increase in mutations is observed at a 16 Å radius, suggesting active mutation sites. This trend continues as the radius extends to 25 Å reflecting an increase in the relative mutation frequency due to the inclusion of more residues. The analysis also highlights a decreasing trend in the relative mutation frequency of viral mutations over time, suggesting that the widespread use of PAXLOVID, as a primary treatment, plays an important role in combating COVID-19. It is important to note that the data in Figure 2e represents the times of public data release, typically delayed by about a month from the actual data collection. During the peak of PAXLOVID’s usage in July 2022 [2], an anomaly is observed - a significant rise in the relative mutation frequency, as represented by the green line. This suggests that heavy

drug use may enhance mutations at active residues, potentially leading to drug resistance. As shown in Figure 2f, it offers an extended analysis focusing on the domain within a radius of 16 Å from the drug. Here, the PRO residue of SARS-CoV-2 M^{Pro} is identified as the most active in mutation frequency, aligning with the sharp increase observed in Figure 2e. This insight is crucial for understanding the mechanisms behind the observed mutation patterns and the potential challenges in combating drug resistance.

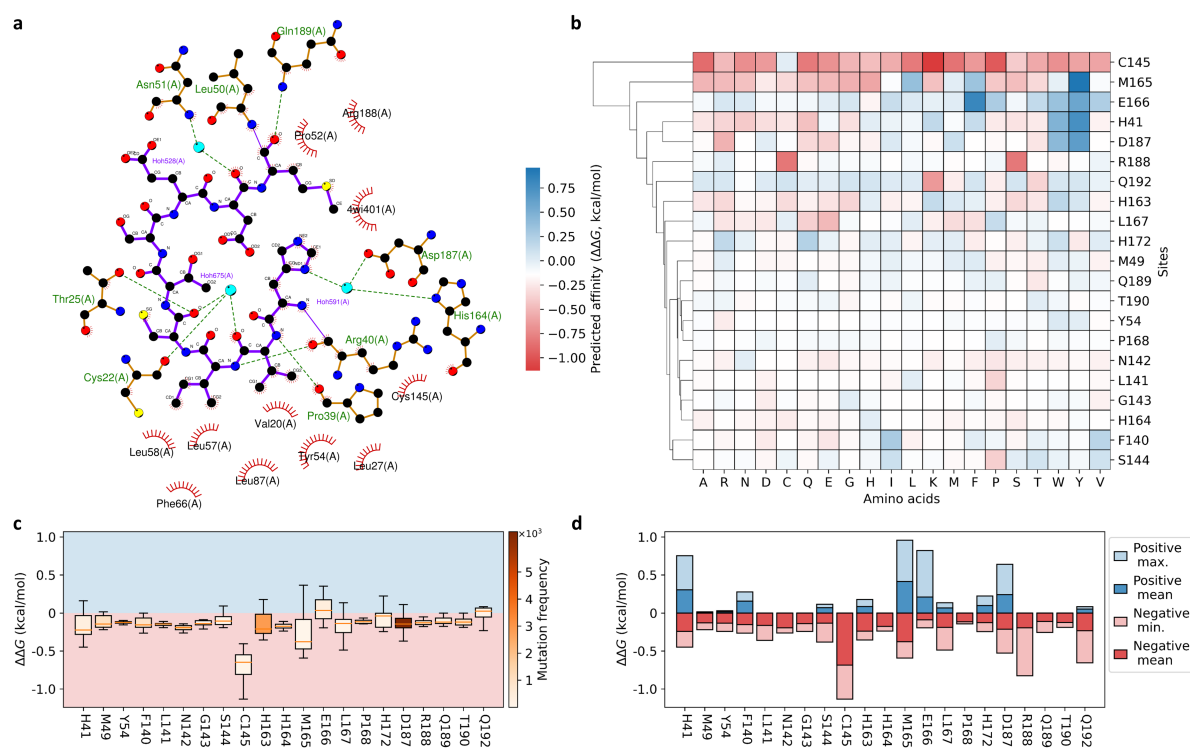


Figure 3: Analysis of predicted mutation induced affinity changes in the SARS-CoV-2 M^{Pro}-PAXLOVID complex. **a**, 2D representation of interaction schematic between SARS-CoV-2 M^{Pro} and PAXLOVID. It highlights 22 residues in proximity to PAXLOVID. **b**, The heatmap illustrates the effects of single-point mutations on binding affinity ($\Delta\Delta G$) for 21 residues near PAXLOVID. For each residue, 19 possible mutations are considered, with predicted affinity changes color-coded from red (negative change) to blue (positive change). **c**, The box chart displays the predicted changes in binding affinity ($\Delta\Delta G$, kcal/mol) for the original SARS-CoV-2 M^{Pro}-PAXLOVID complex when single-point mutations are introduced to the 21 labeled residues (as shown in **a**). Each residue is substituted with the other 19 possible amino acids to measure the effect. The light blue background indicate a positive affinity change, while the light red background indicate a negative change. The intensity of the box color signifies the strength of the mutation frequency. **d**, The bar plot presents the range of mutation-induced affinity changes ($\Delta\Delta G$) for all possible mutations at each site. Maximum and average positive $\Delta\Delta G$ values are shown in light and dark blue, respectively, while minimum and average negative $\Delta\Delta G$ values are depicted in light and dark red. Positive $\Delta\Delta G$ values strengthen binding, whereas negative values weaken it for each complex.

The potential drug resistance in the SARS-CoV-2 main protease is a critical challenge to the efficacy of therapeutic strategies, particularly with the use of PAXLOVID. To enhance our understanding and develop strategies to combat potential drug resistance, our study involves a meticulous single-point mutation scanning around the drug-binding site of the protease. We focus on 21 key residues of the SARS-CoV-2 main protease that are essential to this investigation. Utilizing the

PLFormer model, fine-tuned on the SARS-CoV-2 BA set and validated through a 5-fold cross-validation approach, we predict the binding affinity changes resulting from these mutations. To be note, the Gibbs free energy (ΔG), measured in kcal/mol, serves as a critical indicator of favorable binding interactions within drug-target relationships. The transformation from the inhibition constant (K_i) to ΔG is quantified by the equation $\Delta G = -RT \ln K_i \approx 1.3633 \times \log_{10} \ln K_i$ (kcal/mol). Utilizing training data from PDBbind [23, 24, 25, 26], the binding affinity for protein-ligand complexes is labeled as $L = -\log_{10} \ln K_i$, where a higher L value denotes stronger protein-ligand interactions, leading to the approximation $\Delta G \approx 1.3633 \times -L$. The binding affinity for the wild-type virus-drug complex is represented by ΔG_{WT} , while that for the mutated virus-drug complex is denoted by ΔG_{Mutant} . Changes in binding affinity are calculated using $\Delta\Delta G = \Delta G_{WT} - \Delta G_{Mutant}$, where a positive $\Delta\Delta G$ indicates a mutation that strengthens the binding affinity between the protein and ligand, and a negative $\Delta\Delta G$ suggests a mutation that weakens these interactions. In this work, the comprehensive validation for PLFormer has provided in the following sections.

Figure 3a provides a 2D representation of the interactions between SARS-CoV-2 M_{pro} and PAXLOVID, highlighting 21 residues in close proximity to the drug. In our analysis, each residue is considered for 19 possible mutations. The PLFormer models independently predict the mutations’ binding affinities, and the averaged results are used to calculate the binding affinity changes, $\Delta\Delta G$. Notably, only the PLFormer model is employed for this task, as sequence-based models may not effectively discern the subtle differences caused by single-point mutations. Figure 3b color-codes the binding affinity changes, with red indicating negative changes and blue indicating positive changes. The corresponding quantitative predictions of $\Delta\Delta G$ are listed in Table 7. From our analysis, it is revealed that mutations at residue C145 significantly reduce the binding affinity in the SARS-CoV-2 M^{pro} -PAXLOVID complex. However, it’s important to note that mutating cysteine at this site is challenging due to the indispensable role of its thiol group, which is crucial for forming disulfide bonds and maintaining the protein’s structural and functional integrity. Despite this, historical data indicate that 6 actual mutations have occurred at this site: C to S twice, C to Y three times, and C to F once. So in our DMS process, we methodically induced mutations at C145, exploring all potential alterations. These artificially induced mutations, while designed for comprehensive analysis, may not accurately reflect naturally occurring evolutionary changes due to the critical functional and structural roles of C145. The marked decrease in affinity, as predicted, likely result from the disordered or compromised structural integrity following these mutations. This observation underscores the PLFormer-PAF model’s ability to accurately capture and reflect fundamental biological principles during its training, effectively demonstrating the significant impact of specific amino acid residues on protein-ligand interactions.

Further, Figure 3c displays the statistical results of affinity changes as a box chart. The majority of mutations exhibit a negative impact on binding affinity (19 out of 21), suggesting a weakening effect on PAXLOVID’s functionality. In addition, the distribution of mutation frequencies across various residues is illustrated using a color-coded scheme, as indicated by the colorbar. A particularly noteworthy observation is the exceptionally high mutation frequency at residue D187, recorded at 6489 mutations as of November 29, 2023. This high frequency is attributed to the virus’s adaptive mechanism aimed at circumventing drug effects, resulting in mutations that potentially weaken the drug’s efficacy. The mutation at D187 notably aligns with the predicted outcome where the predicted mutations lead to a negative average binding affinity change ($\Delta\Delta G < 0$).

This pattern is consistent across the majority of observed sites, where high mutation frequencies are typically associated with negative average binding affinity changes. Contrarily, only two out of the twenty-one analyzed sites exhibit a positive average binding affinity change. These sites, E166 and Q192, demonstrate lower mutation frequencies of 3 and 9, respectively. Recently, Clayton et al. [3] investigated the H172Y mutation in SARS-CoV-2 M^{pro} , uncovering its role in drug resistance by noting a 1.9 kcal/mol decrease in binding affinity experimentally. Free energy perturbation (FEP) simulations estimated a 2.3-2.7 kcal/mol reduction, while empirical calculations showed a 0.3 kcal/mol decrease. Our PLFormer model’s prediction of a 0.24 kcal/mol reduction aligns with these findings, despite being quantitatively smaller. This consistency underscores the PLFormer-PAF’s capability to mirror experimental outcomes with commendable accuracy, especially under high-throughput scanning conditions. Further analysis, depicted in Figure 3c, illustrates the distribution of predicted binding affinity changes in H172 across 19 mutations. The 75th percentile falls below 0, indicating a predominance of mutations leading to a reduction in the interactions between the virus and the drug.

In an effort to emphasize the most significant changes in affinity at each site, Figure 3d details both the maximum increases and the minimum decreases in binding affinity. From this analysis, it is evident that the majority of the sites, specifically 16 out of 21, exhibit changes that predominantly diminish the efficacy of the Pfizer drug. In addition to these extremes, the figure also offers a comprehensive view of the average shifts in binding affinity, both positive and negative, at each site. The data suggest that while most sites are predisposed to mutations that weaken the drug’s binding affinity, there are a select few that demonstrate a marginal enhancement in affinity. These findings underscore the critical nature of the interaction sites surrounding the drug, highlighting that even minor mutations at these locations can have significant implications and thus warrant meticulous surveillance. Furthermore, detailed statistical metrics of $\Delta\Delta G$, such as the average, median, standard deviation, first quartile, and third quartile for each residue, are systematically tabulated in Table 5. Additionally, the maximum $\Delta\Delta G$, minimum $\Delta\Delta G$, mean value of positive $\Delta\Delta G$, and mean of negative $\Delta\Delta G$ for each residue are comprehensively listed in Table 6.

2.3 Evaluating PLFormer on PDBbind benchmarks.

The prediction of protein-ligand binding affinity plays a pivotal role in fighting against COVID-19. To assess the scoring capability of our models, we first finetuned the pretrained PLFormer by using the latest PDBbind v2020 general set. Because there is no independent test set from PDBbind v2020 dataset, we evaluated the model by using the three most widely recognized protein-ligand datasets from the of PDBbind database, including the core set of CASF-2007, CASF-2013, and CASF-2016 [25, 24, 26]. Here, the training set from PDBbind v2020 general set is excluding the overlap from three core sets mentioned above. The Pearson correlation coefficient (PCC), the mean absolute error (MAE), and the root mean squared error (RMSE) are used to measure the performance of the scoring function during the comparison. For the kcal/mol unit conversion, one need to multiply the predicted values by 1.3633 in the predictions because of the binding affinity of datasets were measured by $-\log K_d/K_i$. In this task, the PLFormer was fed with an input path topological sequence of length 100, employing filtration parameters at 0.1 intervals spanning from 0 Å to 10 Å. The topological analysis encompasses a domain extending up to 20 angstroms, centered at the ligand.

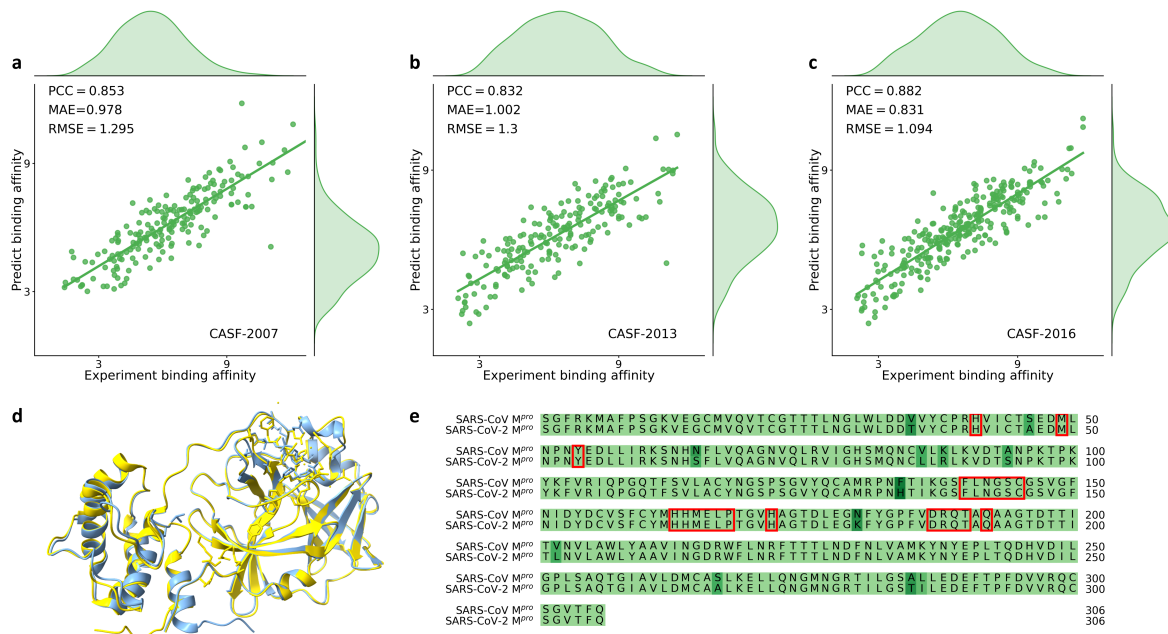


Figure 4: Performance of PLFormer-based model on protein-ligand complex binding affinity prediction. **a-c**, The correlation between the binding affinities predicted by PLFormer-Seq (in kcal/mol) and the experimental outcomes for three separate benchmarks: CASF-2007, CASF-2013, and CASF-2016. **d**, 3D conformation alignment of SARS-CoV-2 (blue, PDBID: 7VH8) and SARS-CoV (yellow, PDBID: 2A5I) main proteases, the structures are from . **e**, 2D sequence alignment of SARS-CoV-2 and SARS-CoV main proteases, the color intensity indicates the difference between two sequences. The specific residues, which are involved in interactions between the virus and the drug, are highlighted with red rectangles.

To ensure robustness in our analysis, we initially trained 20 instances of the PLFormer, each initialized with a distinct random seed. This approach aims to minimize errors potentially stemming from the initialization process. Additionally, to offset any biases associated with relying solely on a single model framework, we have incorporated sequence-based models into our methodology. Specifically, we utilize the ESM model [27] to extract embedded protein features, and the Transformer-CPZ model [28] for extracting SMILES features. Based on these sequence-based features, we subsequently train 20 Gradient Boosting Regressor Trees (GBRT) models, referred as Seq-MLs. For the final analysis, we apply a consensus method that involves selecting a random subset of 10 models from both the 20 PLFormers and the 20 Seq-MLs. The average of the predictions from these selected models, which we term PLFormer-Seq, constitutes our final predictive model. To validate the efficacy of this approach, we performed an extensive evaluation on the CASF-2007, CASF-2013, and CASF-2016 core sets, averaging the results over 400 repetitions for each dataset.

In the evaluation of the PLFormer-based models, as shown in Figure 4, we compared the predicted protein-ligand binding affinities with experimental results, employing PCC, MAE, and RMSE as performance metrics. The model demonstrated remarkable consistency across multiple benchmarks: for CASF-2007, CASF-2013, and CASF-2016, it achieved average PCCs of 0.853, 0.832, and 0.882, and RMSEs of 1.295, 1.3, and 1.094, respectively. Additional comparisons for both Seq-ML and PLFormer predictions with experimental results were illustrated in Figure 8.

Table 1: The performance of recently proposed models is assessed through the evaluation of their PCCs(RMSEs) using various training datasets. To express RMSEs in kcal/mol, a conversion factor of 1.3633 is multiplied the values in the table. Footnote ^a highlights differences in test dataset sizes, including the PDBbind-v2013 core set (N = 180) and the PDBbind-v2016 core set (N = 276). Footnote ^b denotes the use of the PDBbind-v2016 core set (N = 290) as the test dataset.

Model	Training set	CASF-2007 core set	CASF-2013 core set	CASF-2016 core set
Pafnucy [29]	v2016(11906)			0.78
Ligand-based [30]	v2018(11663)	0.836	0.780 ^a	0.821 ^a
graphDelta [31]	v2018(8766)			0.87(1.431) ^b
ECIF [32]	v2019(9299)			0.866(1.594)
OnionNet-2 [33]	v2019(>9000)		0.821(1.850)	0.864(1.587)
DeepAtom [34]	v2018(9383)			0.831(1.680) ^b
SE-OnionNet [35]	v2018(11663)		0.812(2.307)	0.83
Deep Fusion [36]	v2016(9226)			0.803(1.327) ^b
PLFormer-Seq	v2020(18904)	0.853 (1.765)	0.832 (1.774)	0.881 (1.493) 0.883 (1.481) ^b

Despite the challenge of equitably comparing our results with other deep learning models, as detailed in Table 1, our model stands out in the PDBbind v2020 training set with 18,904 protein-ligand complexes. PLFormer achieved compelling results with a PCC of 0.853 and an RMSE of 1.295 (equivalent to 1.769 kcal/mol) on the CASF-2007 core set. For the CASF-2013 core set, the PCC of 0.832 and an RMSE of 1.301 (equivalent to 1.777 kcal/mol) are obtained. Similarly, on the CASF-2016 core set, we obtained a PCC of 0.881 with an RMSE of 1.095 (equivalent to 1.496 kcal/mol). For the PDBbind v2016 core set, we achieved a PCC of 0.883 with an RMSE of 1.086 (equivalent to 1.483 kcal/mol). Notably, our model consistently outperformed others in PCC scores across all benchmarks, with the lowest RMSEs, except for graphDelta’s reported RMSE of 1.05. However, it is noteworthy that our results represent the average of 400 repetitions, in contrast to graphDelta’s evaluation, which was based on a single model selected at 2000 epochs, potentially leading to variability in performance. These results underscore the robustness and predictive power of the PLFormer model in protein-ligand binding affinity predictions, marking it as a state-of-the-art tool in the field.

2.4 Evaluating PLFormer on SARS-CoV(-2) BA dataset.

To enhance the predictive capabilities of our PLFormer model in addressing challenges related to SARS-CoV-2 M^{pro} , such as drug resistance to the Pfizer drug PAXLOVID, we have incorporated a comprehensive dataset. This dataset, denoted as the SARS-CoV(-2) BA set, includes information on 155 inhibitors that are effective against the main protease of either SARS-CoV or SARS-CoV-2. The specifics of this dataset are elaborated in Table 3. The rationale behind including both SARS-CoV and SARS-CoV-2 related complexes in the SARS-CoV-2 BA set stems from their high structural similarity. This similarity is visually substantiated in Figure 4e, where the 3D structures of SARS-CoV M^{pro} and SARS-CoV-2 M^{pro} are compared. The overlapping structures underscore

their resemblance, providing a solid basis for using data from both viruses to inform our model. Further reinforcing this approach is the evidence presented in Figure 4e, which depicts the 2D sequence alignment of the main proteases of both viruses. This alignment highlights the high degree of sequence conservation, with most sites being identical and only a few exhibiting significant differences (dark green). By integrating data related to SARS-CoV M^{pro} , the PLFormer is better equipped to understand the intricate relationships between inhibitors and SARS-CoV-2 M^{pro} . This understanding is crucial for predicting the behavior of SARS-CoV-2 M^{pro} , especially in the context of emerging drug resistance scenarios. Thus, the inclusion of this comprehensive dataset is a strategic step towards refining the accuracy and reliability of our predictive model.

Specifically, the introduced SARS-CoV(-2) BA set is driven from the original SARS-CoV set in the previous work, which includes 185 inhibitors [37]. From this set, we excluded inhibitors that overlapped with those in the PDBbind v2020 training set, resulting in a final count of 155 inhibitors. For validation purposes, the SARS-CoV BA set was divided into five distinct, non-overlapping folds, each containing 31 protein-ligand complexes. In the fold prediction task, PLFormer-Seq was trained on four folds and tested on the remaining one, ensuring no overlap between training and testing sets. The training for PLFormer was based on a version of the PLFormer model previously fine-tuned on the PDBbind-v2020 dataset. To enhance the robustness of our results, we trained 20 models for each fold prediction task. The final prediction for each fold was determined by averaging the predictions from these 20 models.

Table 2: 5-fold cross validation performance of of PLFormer-Seq model on SARS-CoV(-2) BA set. The RMSE and MAE are measured in kcal/mol

Folds	1	2	3	4	5	Average
PCC	0.549	0.824	0.684	0.674	0.659	0.678
RMSE	1.393	0.972	1.283	0.995	0.997	1.128
MAE	1.148	0.8	0.983	0.772	0.829	0.906

Table 2 reveals the performance for each fold prediction task. Their averaged performances on test data across 5-fold of the SARS-CoV(-2) BA set are found to be PCC = 0.678, RMSE = 1.128 kcal/mol, and MAE = 0.906 kcal/mol. These results endorse the reliability of these models in the binding affinity prediction for SARS-CoV/SARS-CoV-2 related inhibitors. The comparison of the predicted binding affinities from PLFormer-Seq, PLFormer model, and Seq-ML model with true labels in 5-fold cross validation is shown in Figure 9. With these promising results, it is encouraging to carry out PLFormer models to predict the binding affinity changes of mutated SARS-CoV-2 with drug PAXLOVID. It is worth noting that if the 5-fold cross-validation is conducted on a very small datasize. The training size for each fold prediction is only 124, the averaged PCC=0.688, suggests a positive correlation between the predicted and actual values, indicating that the model has learned meaningful patterns and relationships within the data, suggesting that our model can effectively leverage pre-trained knowledge to achieve substantial performance even with constrained data resources.

Table 2 presents the performance metrics for each fold in the 5-fold cross-validation on the SARS-CoV-2 BA set. On average, the models achieved a PCC of 0.678, a RMSE of 1.128 kcal/mol, and a MAE of 0.906 kcal/mol. These results demonstrate the models’ capability in accurately

predicting binding affinities for inhibitors related to SARS-CoV and SARS-CoV-2. A comparative analysis of the predicted binding affinities by PLFormer-Seq, the baseline PLFormer model, and the Seq-ML model against actual values is depicted in Figure 9. The promising outcomes from this analysis suggest that PLFormer models hold potential for predicting binding affinity changes in mutated strains of SARS-CoV-2, such as those interacting with the drug PAXLOVID. It is important to highlight that these results were obtained from a relatively small dataset. Each fold in the 5-fold cross-validation process involved training on only 124 data points. Despite this limitation, the models still achieved a respectable average PCC of 0.688. This suggests a significant positive correlation between predicted and actual binding affinities, indicating the models’ ability to discern relevant patterns and relationships within the data. The success of the models under these constrained data conditions underscores their effectiveness in leveraging pre-trained knowledge to deliver robust performance, even when data availability is limited.

3 Discussion

In this section, we focus on two key aspects. First, we demonstrate the PLFormer-PAF’s capability in accurately predicting binding affinity changes due to single-point mutations in SARS-CoV-2, particularly in relation to the Pfizer drug PAXLOVID. Second, we explore how the PLFormer model, utilizing persistent path Laplacian method, enhances our understanding of protein-ligand interactions.

In this study, the proposed PLFormer-PAF stands out as a groundbreaking framework in computational biology and drug discovery. It is distinctively divided into two synergistic strategies: (1) Historical Data Analysis Strategy, and (2) Predictive Modeling Strategy. The essence of PLFormer-PAF’s effectiveness lies in the integration of these approaches. The Historical Data Analysis Strategy harnesses factual insights generated from a rich array of sources, including the GISAID database, alongside advanced sequencing and genotyping techniques. These insights are not just foundational in constructing accurate predictive models but also play a crucial role in validating and refining these models. By cross-referencing predictive outcomes with historical data, PLFormer-PAF significantly boosts its reliability and accuracy. Furthermore, Predictive Modeling Strategy of PLFormer-PAF adeptly tackles key challenges in binding affinity predictions. This includes the need for precise modeling of complex molecular interactions and effective prediction of drug efficacy. Notably, the PLFormer-PAF’s predictions reveal a significant trend: mutations near the drug-binding sites often lead to a decrease in drug efficacy, highlighting the critical issue of drug resistance caused by such mutations. This observation is particularly relevant in the context of widely used antiviral medications, such as PAXLOVID. The PLFormer-PAF’s analysis supported by real-world data, where an abnormal increase in relative mutation frequency was observed during the extensive use of PAXLOVID in July 2022, as illustrated in Figure 2e. This suggests that the virus tends to develop mutations that weaken the drug’s effectiveness. The insights provided by PLFormer calls for cautious administration of antiviral drugs in clinical settings. Moreover, it is imperative to closely monitor mutations around drug-binding sites. Although these sites are relatively stable, any alterations could significantly impact treatment effectiveness. This analysis is not only crucial for developing new treatments or adapting existing ones to counter evolving viral strains but also plays a vital role in informing clinical decisions and shaping public health strategies in the

ongoing fight against COVID-19 or future virus. The PLFormer-PAF thus emerges as an invaluable tool in anticipating and responding to the challenges posed by rapidly evolving pathogens. The fusion of deep learning with data analytics in PLFormer-PAF not only deepens our comprehension of current drug interactions but also opens avenues for identifying novel therapeutic targets.

For the PLFormer, we introduce the Persistent Path Laplacian (PPL) method [18] for advanced representation of 3D protein-ligand complexes, surpassing traditional graph and simplicial complex methods. In particular, the path topological sequence embedding module within PLFormer utilizes path complexes to model intricate molecular interactions, accommodating complex relationships by connecting vertices across multiple dimensions and incorporating orientations to encode physical and chemical properties. Specifically, the Figure 12 showcases path complex representations for a multi-elemental system, specifically two $B_7C_2H_9$ isomers, highlighting the capacity to capture different elemental configurations through the directionality of corresponding paths. This approach enhances the representation of various elemental configurations in complex systems. Additionally, we integrate PPL for a comprehensive analysis of these complexes' geometric and topological characteristics. This method draws on concepts from physical systems, such as the correlation of the Laplacian matrix with kinetic energy in quantum mechanics, to provide insightful analysis through Laplacian eigenvalues [38]. Our approach enables a deeper understanding of the structural and energetic properties of complex molecular systems, aligning with fundamental principles in physics.

In comparison to traditional persistent homology theory, the PPL introduced in this study marks a significant advancement over traditional persistent homology theory in analyzing protein-ligand complexes. Unlike the latter, which is limited to simplicial complexes, the PPL within PLFormer effectively analyzes path complexes, a more general concept encompassing traditional graphs, digraphs, and simplicial complexes. It offers a comprehensive characterization of these complexes, capturing not only fundamental homology information like Betti numbers but also providing geometric insights and homotopic shape evolution through the non-harmonic spectra of persistent path Laplacians. This is illustrated in our analysis of protein-ligand complexes, where the PLFormer encompasses traditional homology analysis, as shown in Figure 10.

Moreover, the PLFormer introduces persistence, allowing for a multiscale characterization of atomic interactions within protein-ligand complexes. This approach captures interactions at various scales, from covalent and ionic bonds to van der Waals forces and to hydrophobic effects, guiding transformer models to understand the distinct contributions of each scale to properties like binding affinity. It offers a topological sequence that evolves with changing scales, crucial for fine-tuning in computational models. Additionally, our study acknowledges the myriad of elemental interactions, such as hydrogen bonding, van der Waals forces, and ionic, polar, nonpolar, and hydrophobic interactions, crucial in molecular stability and specificity. To capture these diverse interactions, we introduce an element-specific analysis within the PLFormer framework. This involves constructing sub-path complexes based on common heavy elements in proteins and ligands, leading to the creation of element-specific Laplacian matrices for each sub-path complex. This technique enriches the extraction of physical and chemical features, enhancing the transformer model's ability to comprehend the complex dynamics of protein-ligand interactions under both self-supervised and supervised learning paradigms. Further details on this element-specific analysis are provided in the Method Section 4.

4 Methods

4.1 Datasets

In this study, we employed a diverse dataset for pre-training, which comprises protein-ligand complexes sourced from the extensive PDBbind database, including CASF-2007, CASF-2013, CASF-2016, and PDBbind v2020 [23]. To ensure data integrity and eliminate redundancies, we conducted a rigorous curation process, resulting in 19,513 non-overlapping complexes for pre-training. For training and testing, we followed a rigorous approach. Since PDBbind v2020 lacks a core set, we used the core sets from CASF-2007, CASF-2013, and CASF-2016 as our testing set. The general set (containing 19,443 complexes) from PDBbind v2020, with the exclusion of the core sets from CASF-2007, CASF-2013, and CASF-2016, served as our training set (18,904) for the PLFormer model. Comparative results with models trained on different data sources are available in Table 1.

Additionally, our study includes the extra inhibitors of SARS-CoV/SARS-Cov-2 M^{Pro} collected by Nguyen et al. [37]. We excluded overlapping complexes from PDBbind-v2020, resulting in 155 complex structures with corresponding binding affinities, which were used to independently validate the proposed PLFormer. To investigate the impact of mutations in the SARS-CoV-2 main protease when interacting with the FDA-approved drug PAXLOVID (PDBID: 7VH8), we considered 21 interaction residues around the drug [20]. For each residue, we explored 19 possible mutations, resulting in a total of 399 single-site mutated protein-ligand complexes. Together with the original complex, our study encompasses 400 unique protein-ligand complexes, referred as SARS-CoV-2 MM. Specifically, the proteins with mutations are systematically generated using the Jackal software package [39]. In this process, each mutant variant is created by substituting a single residue from the wild-type protein, utilizing the side-chain alteration capabilities of the Jackal package. Subsequently, the Profix software is employed to refine the dataset, ensuring the removal of anomalies and enhancing data quality for further analysis. Finally, we used the Protein Preparation Wizard function of Schrödinger software for energy minimization [40], rectifying unreasonable atomic positions and ensuring stability and reliability in the protein-ligand complex structures. Further details regarding the data can be found in Table 3.

In this work, we analyzed mutation frequency data derived from GenBank, the first platform to publish the complete genome sequence of SARS-CoV-2 in January 2020 [41]. This initial release marked the beginning of a rapid influx of SARS-CoV-2 genome sequences globally. Our data collection and analysis process is methodical and includes the following steps: (1) Data Acquisition: We systematically download all complete, high-coverage SARS-CoV-2 genome sequences from infected individuals around the world. These sequences are obtained from the GISAID database [42] (<https://www.gisaid.org/>). (2) Quality Control: We rigorously filter out any genome sequences from GISAID that are incomplete or do not have accurately recorded submission dates. (3) Sequence Alignment: The complete genome sequences are aligned with the reference SARS-CoV-2 genome. This alignment is conducted using Clustal Omega [43], employing its default settings for multiple sequence alignment (MSA). Our dataset is extensive, encompassing 3,694,942 complete SARS-CoV-2 genome sequences as of November 29, 2023. To investigate the evolution of drug resistance in the virus, we included genome sequences from key dates throughout 2022: May 10, June 10, August 30, September 30, October 31, and December 31. These specific dates allow us to track and analyze the genetic changes in the virus over time and assess their potential impact on

Table 3: Detailed information of the used datasets.

Data name	Data size	Descriptions	References
Pre-training set (CASF-2007, CASF-2013, CASF-2016, PDBind v2015, PDBind v2020)	19513	The combined PDBbind database, duplicates were removed, and binding affinities were not utilized during the pretraining.	[23, 24, 25, 26]
PDBind v2020	18904	The general set from PDBbind v2020 but had to exclude the core sets from CASF-2007, CASF-2013, and CASF-2016.	[23, 26]
CASF-2007 core set	195	CASF-2007 core set from PDBbind database.	[24, 23]
CASF-2013 core set	195	CASF-2013 core set from PDBbind database.	[25, 23]
CASF-2016 core set	285	CASF-2016 core set from PDBbind database.	[26, 23]
SARS-CoV(-2) BA	155	Inhibitors of SARS-CoV and/or SARS-CoV-2 main protease with corresponding binding affinities, abbreviated as SARS-CoV(-2) BA.	[37]
SARS-CoV-2 MM	400	One complex involves the SARS-CoV-2 main protease interacting with the FDA-approved drug PAXLOVID (PDBID: 7VH8). An additional 399 single-site mutations were created using the 21 interaction sites around the ligand. For each site, we considered 19 possible mutations, resulting in a total of 399 single-site mutated protein-ligand complexes, abbreviated as SARS-CoV-2 MM.	(Current work)

the effectiveness of treatments.

4.2 Path topological sequence embedding

Path and path complex. A path complex is a conceptual generalization of graphs, directed graphs, and simplicial complexes. It is composed of sequences of distinct elements from a finite set, referred to as paths, which serve as its basic building blocks [44, 45]. Figure 5b showcases examples of paths with varying lengths, such as 0-path, 1-path, 2-path, and 3-path. These sequences are similar to the simplices found in a simplicial complex. To draw a parallel, Figure 5c depicts

the 0-simplex (a single node), 1-simplex (a line segment), 2-simplex (a triangle), and 3-simplex (a tetrahedron). For those seeking a deeper understanding of the commonly used graph and simplicial complex structures, additional information can be found in the Supplementary Information, specifically in Section A.3.

In mathematical terms, an *elementary p -path*, or simply p -path, on a non-empty finite set V is a sequence $i_0i_1 \dots i_p$ composed of elements from V , for any non-negative integer p . Let \mathbb{K} denote a field, and $\Lambda_p = \Lambda_p(V)$ be the \mathbb{K} -vector space formed by all p -paths. Any p -path v can be represented as:

$$v = \sum_{i_0, i_1, \dots, i_p \in V} a^{i_0i_1 \dots i_p} e_{i_0i_1 \dots i_p}, \text{ where } a^{i_0i_1 \dots i_p} \in \mathbb{K}.$$

For every integer $p \geq 0$, there is a \mathbb{K} -linear map $\partial : \Lambda_p \rightarrow \Lambda_{p-1}$. This map is defined such that $\partial e_{i_0} = 0$ for $e_{i_0} \in \Lambda_0$, and for $p \geq 1$, $\partial e_{i_0i_1 \dots i_p} = \sum_{k=0}^p (-1)^k e_{i_0 \dots \widehat{i}_k \dots i_p}$, where \widehat{i}_k indicates the omission of the index i_k . Direct verification confirms that ∂ acts as a boundary operator on the sequence $(\Lambda_p)_p$, fulfilling the condition $\partial^2 = 0$.

A *path complex* on a non-empty finite set V is formally defined as a non-empty collection \mathcal{P} comprising elementary paths on V . This collection is characterized by the condition that if an elementary path $i_0i_1 \dots i_p$ belongs to \mathcal{P} , then the subsequences $i_0i_1 \dots i_{p-1}$ and $i_1i_2 \dots i_p$ must also be part of \mathcal{P} . Importantly, a simplicial complex can be considered a specific instance of a path complex. The set of paths in a directed graph G forms a path complex, symbolized as $\mathcal{P}(G)$. The paths contained within \mathcal{P} are termed *allowed paths*. This can be represented mathematically as:

$$\mathcal{A}_p = \mathcal{A}_p(\mathcal{P}) = \left\{ \sum_{i_0, i_1, \dots, i_p \in V} a^{i_0i_1 \dots i_p} e_{i_0i_1 \dots i_p} \mid i_0i_1 \dots i_p \in \mathcal{P}, a^{i_0i_1 \dots i_p} \in \mathbb{K} \right\}. \quad (1)$$

By convention, $\mathcal{A}_{-1} = 0$ is used to denote the null space. The set of ∂ -invariant p -paths is defined as follows:

$$\Omega_{-1} = 0, \quad \Omega_p = \Omega_p(\mathcal{P}) = \{x \in \mathcal{A}_p \mid \partial x \in \mathcal{A}_{p-1}\}, \quad \text{for } p \geq 0. \quad (2)$$

Then, Ω_p forms a chain complex, specifically designed to investigate the topological characteristics of path complexes. It is important to note that this chain complex Ω_p becomes simplified when the path complex is reverted to a simplicial complex. The translation of C_α atoms in protein (PDBID: 1MYL, Figure 5d) into a corresponding simplicial complex is illustrated in Figure 5f. In this figure, light blue triangles indicate 2-simplices, while dark blue elements represent 3-simplices, approximately visualizing the alpha helix structures. At the same time, the graph representation in Figure 5e only shows the low dimensional information (1-simplices). Additionally, Figure 5g shows the 3-paths within the path complex, marked with arrows against a yellow background, offering an alternate depiction of the alpha helix in the structure. Figure 11 further showcases various topological representations, including graphs, simplicial complexes, and path complexes. For more comprehensive explanations and definitions regarding graphs, simplicial complexes, and path complexes, readers are directed to the Supplementary Information (refer to Section A.3) and earlier publications [44, 45, 18].

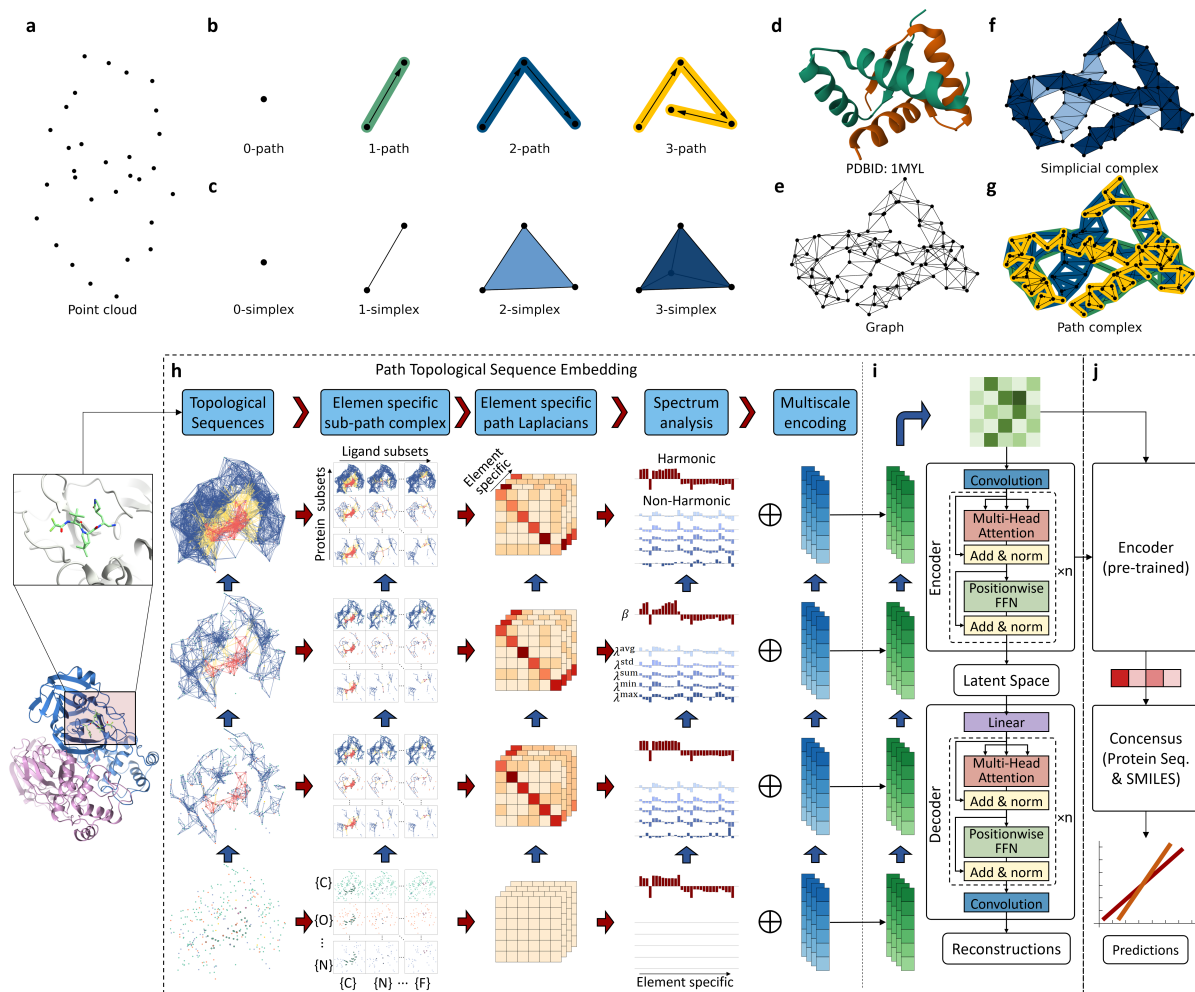


Figure 5: Conceptual illustrations of PLFormer. **a**, Point cloud representations for a structural data. **b**, Illustration of the basic elements of a path complex are illustrated, including 0-path, 1-path, 2-path, and 3-path. **c**, Depiction of the fundamental components of a simplicial complex, including 0-simplex (node), 1-simplex (edge), 2-simplex (triangle), and 3-simplex (tetrahedron). **d**, Visualization of protein 1MYL, featuring only C_{α} atoms. **e**, Graph representation for the C_{α} atoms of protein 1MYL at a cutoff distance of $d = 5 \text{ \AA}$. **f**, Simplicial complex representation for the C_{α} atoms of protein 1MYL at a cutoff distance of $d = 5 \text{ \AA}$, with 2-simplices in light blue and 3-simplices in dark blue. **g**, Path complex representations for the C_{α} atoms of protein 1MYL at a cutoff distance of $d = 5 \text{ \AA}$. The 1-paths are shown with arrows on a green background, 2-paths with blue, and 3-paths with yellow. **h**, This module begins by processing the interactive domain of a protein-ligand complex, dividing it into a topological sequence known as a chain complex in algebraic topology. Element-specific sub-complexes are then formed to encode physical interactions at various scales, regulated by a filtration parameter. Element-specific Persistent Topological Path Laplacians (PLs) are constructed to extract topological invariants, capturing the shape and stereochemistry of the sub-path complexes. For these subcomplexes, changes in topological invariants across scales are captured in the harmonic spectrum of the path Laplacians, while their homotopic shape evolution across scales is reflected in the non-harmonic spectrum. Finally, these multiscale topological invariants and homotopic shape (stereochemical) evolutions are compiled into a topological sequence, which serves as input for the Transformer. **i**, Self-supervised learning for topological sequences is applied to unlabeled topological sequences in both Encoders and Decoders. The outputs from the reconstructed topological sequences are utilized to compute the reconstruction loss. **j**, Supervised fine-tuning stage: As elaborated in **c**, task-specific protein-ligand complex data are input into the pretrained encoder. Optionally, these predictions can be combined with sequence-based predictions for enhanced accuracy.

Vietoris-Rips path complex and alpha path complex. The Vietoris-Rips (VR) complex and the alpha complex are highly regarded topological models for analyzing sets of data points. In cases where \mathcal{K} is either a VR complex or an alpha complex, the points that comprise a simplex in \mathcal{K} inherently encapsulate geometric information, including both the size and orientation of the set of points. Drawing inspiration from the VR complex and alpha complex, we introduce the Vietoris-Rips (VR) path complex and the alpha path complex, aimed at capturing this geometric information. For describing the geometry of simplices, a weight function $w : \mathcal{K} \rightarrow \mathbb{R}$ and a graded orientation function $\varrho_n : \mathcal{K}_n \rightarrow S_{n+1}$ for $n \geq 1$ are employed. In this context, S_n represents the permutation group with n elements. The VR/alpha path complex is formulated as follows:

$$\mathcal{P}_\eta := \{S \times \varrho_*(S) \mid w(S) \leq \eta, S \in \mathcal{K}\}. \quad (3)$$

The VR/alpha path complex can be viewed as an extension of the conventional VR/alpha complex. It reduces to the standard VR/alpha complex when the functions $w : \mathcal{K} \rightarrow \mathbb{R}$ and $\varrho_n : \mathcal{K}_n \rightarrow S_{n+1}$ are considered to be constant.

In this study, unless explicitly stated otherwise, all analyses are based on the Vietoris-Rips (VR) path complex. Illustrative examples of both the VR path complex and the alpha path complex can be seen in Figures 6 and 7. Comprehensive details on the construction of VR path complexes and alpha path complexes are available in the Supplementary Information, specifically in Section A.4.

Path Laplacians and spectrum analysis. The combinatorial Laplacian is a key instrument in discrete geometry and algebraic topology, providing insights into the structure of various topological systems. These include simplicial complexes, path complexes, hypergraphs, and hyperdigraphs [46, 44, 45]. Analogous to how the graph Laplacian is utilized for examining graph properties (with graphs being equivalent to 1-simplices), the combinatorial Laplacian is employed for exploring attributes of simplicial and path complexes. The eigenvalues of the graph Laplacian reveal connectivity aspects of the graph. For instance, the second smallest eigenvalue, known as the Fiedler vector, indicates the graph’s algebraic connectivity. Similarly, the smallest positive eigenvalue, referred to as the spectral gap, has a significant relation to the Cheeger constant. The entirety of these eigenvalues forms the spectrum of the Laplacian operator.

The Laplacian matrix of a graph is defined as $\mathcal{L} = D - A$, where D is the degree matrix, and A is the adjacency matrix. In the context where the graph is considered as a one-dimensional (1D) simplicial complex, and taking B_1 as the matrix that represents the 1D boundary operator, we find that the graph’s Laplacian matrix can be accurately formulated as $\mathcal{L} = B_1 B_1^T$. This observation paves the way for extending the Laplacian operator to higher dimensions through the use of the boundary operator, culminating in the Laplacian operator for simplicial complexes. Suppose K represents a simplicial complex, and B_k signifies the matrix of its k -dimensional boundary operator. The Laplacian matrix in this context is given by:

$$\mathcal{L}_k = B_{k+1} B_{k+1}^T + B_k^T B_k. \quad (4)$$

In this equation, B_k^T is the transpose of B_k . The expression $B_k^T B_k$ reflects the connectivity stemming from the juncture of k -simplices at $(k - 1)$ -simplices. Conversely, $B_{k+1} B_{k+1}^T$ represents the interactions that occur due to the incorporation of k -simplices into $(k + 1)$ -simplices.

Recall that the topological characteristics of simplicial complexes or path complexes are obtained from their chain complexes. The Laplacian operator can be defined from the perspective of chain complexes. Consider Ω_* as a chain complex (as shown in Equation 2), equipped with the differential $\partial_k : \Omega_k \rightarrow \Omega_{k-1}$. We assume that for each k , Ω_k is endowed with an inner product structure. As a result, the boundary operator ∂_k is paired with its adjoint operator ∂_k^* . The *combinatorial Laplacian* $\Delta_k : \Omega_k \rightarrow \Omega_k$ is then defined as

$$\Delta_k = \partial_{k+1} \circ \partial_{k+1}^* + \partial_k^* \circ \partial_k. \quad (5)$$

Notably, Δ_0 is given by $\partial_1 \circ \partial_1^*$. For each k , upon selecting a standard orthonormal basis for Ω_k , the corresponding representation matrix L_k of the Laplacian operator Δ_k , relative to this basis, is expressed as form in Equation 4, where B_k represents the matrix corresponding to the boundary operator ∂_k , as determined by left multiplication [47].

This combinatorial Laplacian expands upon the graph Laplacian, which primarily addresses properties of graphs, conceptualized as 1-simplicial complexes. In contrast, the combinatorial Laplacian extends the analysis to higher dimensions. Its eigenvalues and eigenvectors reveal significant geometric and topological details about the simplicial or path complex. Given that the Laplacian matrix is positive semidefinite, all its eigenvalues are non-negative. The zero eigenvalues, forming the harmonic spectrum, are particularly informative of the topological structure. Meanwhile, the non-zero eigenvalues, or the non-harmonic spectrum, convey the geometric aspects of the system. In the case of \mathcal{L}_k , the frequency of zero eigenvalues (indicating the number of occurrences of 0 as an eigenvalue) corresponds to the count of independent components and also to the topological invariants (β_k) in the k -dimensional space [48]. For instance, the zero multiplicity for \mathcal{L}_0 (i.e., β_0) represents the count of connected components in the graph (1-simplicial complex), for \mathcal{L}_1 (i.e., β_1) it denotes the number of cycles, and for \mathcal{L}_2 , it signifies the number of cavities. The highest eigenvalue λ_k^{max} of \mathcal{L}_k is bounded by the maximal count d_k of $k + 1$ -simplices sharing a common k -simplex (akin to the maximum degree of the graph for \mathcal{L}_0), so $0 \leq \lambda_k^{max} \leq 2d_k$. The smallest non-zero eigenvalue of \mathcal{L}_k , known as the spectral gap and denoted by λ_k^{min} , reflects the geometric structure of the system. This work utilizes various measures like the multiplicity of zero, the average, the standard deviation, the minimum, the maximum, and the sum of the positive eigenvalues of \mathcal{L}_0 for embedding given topological Laplacians. Additionally, to demonstrate the efficacy of Laplacians of path complexes, also referred to as path Laplacians, two $B_7C_2H_9$ isomers with identical shapes but distinct carbon atom placements are used in a validation study, as depicted in Figure 12. This comparison suggests that path Laplacians can encapsulate a broader range of information than standard Laplacians.

Persistent path Laplacians. Persistent Laplacians, also referred to as multiscale topological Laplacians, emerged from a collection of studies conducted on differential manifold settings [?] and discrete point cloud scenarios [49]. Central to the concept of persistent Laplacians [49, 46, 50], as well as in persistent homology [51, 52], is the process of filtration, which facilitates multiscale representation. This filtration, characterized by the scale parameter denoted as d , is tailored according to the specific data structure under examination. For instance, in the context of point cloud data (as shown in Figure 5a), this parameter typically represents the sphere’s radius (or diameter). By incrementally modifying d , a series of hierarchical data representations can be

obtained, as depicted in Figure 10a. Importantly, these representations extend beyond simplicial complexes to include structures like path complexes [18]. For example, in the context of a distance matrix where matrix elements denote distances between vertices, a filtration operation can be implemented. Here, a cutoff value is designated as the scale parameter, and if the distance between two vertices is less than this cutoff, a path is established. As this cutoff value increases, a sequence of nested graphs is formed, where each graph, corresponding to a lower cutoff value, forms a subset of the graphs generated at higher cutoffs.

Similarly, nested simplicial complexes can be constructed using different complex formulations such as the Vietoris-Rips complex, the Čech complex, and the alpha complex. In this study, the focus is on the Vietoris-Rips complex. Mathematically, these nested simplicial complexes are represented as follows:

$$\emptyset \subseteq K_{d_0} \subseteq K_{d_1} \subseteq \dots \subseteq K_{d_n} = K \quad (6)$$

Here, it holds that for any two values $d_i < d_j$, the complex K_{d_i} is a subset of K_{d_j} . This concept is also applicable to path complex, specifically through the Vietoris-Rips path complex framework, where nested path complexes are formed by defining paths in a particular manner [46]. To illustrate the impact of varying filtration parameters, Figure 10a demonstrates changes in point cloud connectivity from Figure 5a, resulting in a progression of path complexes. The methodology for constructing the Vietoris-Rips path complex is detailed in Figure 6. Additionally, this work introduces the concept of the alpha path complex, inspired by the alpha complex, as depicted in Figure 7.

During the progression of a filtration process, a series of chain complexes naturally emerges. Corresponding to each filtration step, denoted as d_i (with i serving as the step index), a distinct chain complex $C(K_{d_i}; G)$ is formed. In mathematical terms, a chain complex associated with a specific filtration step consists of a sequence of Abelian groups (or modules) connected by boundary homomorphisms, which can be represented as follows:

$$\dots \rightarrow C_{k+1}(K_{d_i}; G) \xrightarrow{\partial_{k+1}^{d_i}} C_k(K_{d_i}; G) \xrightarrow{\partial_k^{d_i}} C_{k-1}(K_{d_i}; G) \rightarrow \dots \quad (7)$$

In this sequence, $C_k(K_{d_i}; G)$ denotes the chain group in the k -dimensional space at the specific filtration step d_i .

To provide a broader understanding, we will now present the Laplacian in a more comprehensive mathematical framework. Consider two real numbers, a and b , with $a \leq b$. Let chain complex Ω_*^a is a subset of Ω_*^b . The chain complexes in question could be derived from a variety of sources, such as a filtration of simplicial complexes, path complexes, or hyperdigraphs, to name a few. Additionally, it's important to note that both Ω_*^a and Ω_*^b possess compatible inner product structures. Let $\Omega_{k+1}^{a,b}$ be a set containing elements x in Ω_{k+1}^b such that the boundary operator ∂_{k+1}^b applied to x yields an element in Ω_k^a , formally expressed as $\Omega_{k+1}^{a,b} = \{x \in \Omega_{k+1}^b \mid \partial_{k+1}^b x \in \Omega_k^a\}$.

The persistent boundary operator, denoted as $\partial_{k+1}^{a,b}$ and mapping from $\Omega_{k+1}^{a,b}$ to Ω_k^a , is defined through the action $\partial_{k+1}^{a,b} x = \partial_{k+1}^b x$ for any x residing in $\Omega_{k+1}^{a,b}$. This operator plays a key role in

understanding the persistent structures within the framework of chain complexes.

$$\begin{array}{ccccc}
\Omega_{k+1}^a & \xrightarrow{\partial_{k+1}^a} & \Omega_k^a & \xrightleftharpoons[\leftarrow{(\partial_k^a)^*}]{\rightarrow{\partial_k^a}} & \Omega_{k-1}^a \\
\downarrow & \nearrow{\partial_{k+1}^{a,b}} & \downarrow & & \downarrow \\
\Omega_{k+1}^b & \xrightarrow{\partial_{k+1}^b} & \Omega_k^b & \xrightarrow{\partial_k^b} & \Omega_{k-1}^b \\
& \nwarrow{\partial_{k+1}^{a,b}} & & & \\
& \Omega_{k+1}^{a,b} & & &
\end{array}
\tag{8}$$

The k -th persistent Laplacian is defined as

$$\Delta_k^{a,b} = \partial_{k+1}^{a,b} \circ (\partial_{k+1}^{a,b})^* + (\partial_k^a)^* \circ \partial_k^a.
\tag{9}$$

It is important to recognize that the harmonic part of $\Delta_k^{a,b}$, denoted as $\ker \Delta_k^{a,b}$, has a natural isomorphism to the (a, b) -persistent homology, expressed as $H_k^{a,b} = \text{im}(H_k(\Omega_*^a) \rightarrow H_k(\Omega_*^b))$ [53]. Essentially, the persistent Laplace harmonic component contains information related to persistent homology. To extract valuable information from each chain complex, spectrum analysis is a viable approach. This involves constructing Laplacian matrices for each ∂_k and ∂_{k+1} and analyzing their spectra (eigenvalues and eigenvectors), which can reveal in-depth information about the topological and geometric attributes inherent in the data at a specific filtration scale. The spectral data often offers a concise and informative representation of the data, facilitating effective comparison and analysis across various scales. The persistent attributes used in this work are exhibited in Figure 10. This approach underscores the multifaceted nature of persistent Laplacians in capturing and representing complex topological and geometric structures.

Element-specific embedding In this study, the path topological embedding method is employed for encoding protein-ligand complexes, aiming to enhance prediction accuracy by better representing the molecular-level interactions between proteins and ligands. The element-specific topological embedding approach [19] is utilized to characterize these interactions.

When analyzing ligands, attention is focused on heavier elements like carbon (C), nitrogen (N), oxygen (O), sulfur (S), phosphorus (P), fluoride (F), chloride (Cl), bromide (Br), and iodine (I). In the context of proteins, the analysis is limited to carbon (C), nitrogen (N), oxygen (O), and sulfur (S). A series of element combinations, ordered in a specific sequence, are then employed to represent the interactions between the protein and the ligand. For proteins, the combinations are denoted as $\mathcal{E}_{\text{protein}} = \{\{C\}, \{N\}, \{O\}, \{S\}, \{C, N\}, \{C, O\}, \{C, S\}, \{N, O\}, \{N, S\}, \{O, S\}, \{C, N, O, S\}\}$. Similarly, the ligand combinations are represented as $\mathcal{E}_{\text{ligand}} = \{\{C\}, \{N\}, \{O\}, \{S\}, \{C, N\}, \{C, O\}, \{C, S\}, \{N, O\}, \{N, S\}, \{O, S\}, \{N, P\}, \{F, Cl, Br, I\}, \{C, O, N, S, F, P, Cl, Br, I\}\}$. In the Element-specific embedding framework, protein-ligand interactions are delineated through the topological links between two distinct sets of atoms: one set from the protein and the other from the ligand. For instance, a configuration like $K_{\{C, N\}, \{S\}}$ signifies a path complex where the carbon (C) and nitrogen (N) atoms are part of the protein, while the sulfur (S) atom is part of the ligand. This Element-specific embedding methodology provides a detailed depiction of interactions, focusing on their spatial arrangements and relationships. It can be characterized by

distance matrix D as follows,

$$D(i, j) = \begin{cases} \|\mathbf{r}_i - \mathbf{r}_j\|, & \text{if } \mathbf{r}_i \in \mathcal{E}_{\text{protein}}, \mathbf{r}_j \in \mathcal{E}_{\text{ligand}} \text{ or } \mathbf{r}_i \in \mathcal{E}_{\text{ligand}}, \mathbf{r}_j \in \mathcal{E}_{\text{protein}} \\ \infty, & \text{other} \end{cases} \quad (10)$$

where the \mathbf{r}_i and \mathbf{r}_j are coordinates for the i th and j th atoms in the set, and $\|\mathbf{r}_i - \mathbf{r}_j\|$ is their Euclidean distance. In the PLFormer model, the focus is on protein atoms that are situated within a 20 Å radius of ligand atoms. This model prioritizes protein-ligand interactions by designating an infinite distance value for atom pairs that are exclusively within the protein or within the ligand. This approach ensures that the model’s attention is directed specifically towards the interactions between protein and ligand atoms. For any given protein-ligand complex under consideration, there are 143 potential combinations (derived from 11 protein sets multiplied by 13 ligand sets). Each combination represents a unique path complex and is subsequently analyzed using the persistent path Laplacian method. This approach allows for an in-depth examination of the various possible interactions within the protein-ligand complex, leveraging the unique properties of each element set to understand the complex interplay between the protein and ligand at a molecular level.

4.3 PLFormer model

Model architecture. In this work, the overall framework is based on the PLFormer, a new topological deep learning model that combines the advantages of Transformer model and the path Laplacian method, as shown in Figure 5h and i. It is true that Transformer [14] architecture offered a groundbreaking technique that leverages attention mechanisms to understand sequential data in various domains [54, 28, 55]. However, it is also true that traditional Transformers that can only based on language-like sequences, such as protein sequences or molecular sequences (SMILESs) in the biology and chemistry fields. Here, drawing inspiration from the Transformer’s design and capabilities, we introduced a path topological sequence embedding module, as shown in Figure 5h, to makes it possible to uniquely transfer the intricate 3D protein-ligand complexes into sequences of topological invariants and homotopic shape and also the stereochemical evolution. Specifically, this path topological sequence embedding module sequentially embeds the physical, chemical, and biological interactions of 3D protein-ligand complexes at various scales into a topological sequence, containing topological invariants and homotopic shapes, admissible to the transformer architecture. Pretraining on a diverse set of protein-ligand complexes empowers the model to grasp the broad characteristics and nuances of molecular interactions, including various stereochemical effects that cannot be captured by traditional molecular sequences. Subsequent fine-tuning on specific datasets ensures that the output embeddings for each complex not only capture the intrinsically intricate interactions within the complex but also represents the traits of the complex in contact with the whole dataset, which facilitates the downstream deep learning and improves the prediction accuracy.

To focus the analysis on a specific domain of the protein-ligand complex, we first identify a targeted area, as highlighted in the left of Figure 5h. This process begins by pinpointing all heavy ligand atoms and the proximate protein atoms, defining the domain with a 20 Å cutoff radius from the ligand. Subsequently, to transfer 3D structures to a format suitable for analysis, the PLFormer employs its unique path topological sequence embedding module, illustrated in Figure 5h. This module utilizes a multiscale approach, akin to a filtration process in algebraic topology, to transform these 3D structures into path topological sequences. Specifically, the scale range spans from 0 Å

to 10 Å in 0.1 Å increments, leading to a path topological sequence of 100 units. At each filtration step, the embedded features are represented in a 143 by 6 matrix, with 6 attributes for each \mathcal{L}_0 . The path topological embedding module’s output is a summation of these topological embeddings and trainable multiscale embeddings (see Figure 5h). To reshape the 143 by 6 matrix at each filtration step into a 1-dimensional vector, the model incorporates a convolutional layer in both the Transformer’s encoder and decoder (illustrated in Figure 5i). This transformation is achieved through the innovative Persistent Path Laplacians (PPLs) technique. PPLs not only capture the spatial organization but also integrate diverse physical, chemical, and biological interaction features into element-specific PPLs. The result is a series of embedding vectors, generated through the comprehensive multiscale analysis of PPLs. A detailed exposition of this path topological sequence embedding module is provided in the methods section 4.2.

PLFormer leverages the rich diversity of unlabeled protein-ligand complexes through a self-supervised pretraining phase, as depicted in Figure 5i. Central to this phase is the Transformer encoder-decoder architecture. The decoder in this architecture is specifically tasked with reconstructing the path topological sequence embeddings from their encoded counterparts. The effectiveness of this reconstruction process is assessed by comparing the output embeddings with the original input, ensuring fidelity in the learning process. This self-supervised approach, devoid of labeled data, uniquely positions the model to intuitively grasp the complex dynamics inherent in protein-ligand interactions. Following this pretraining, the model transitions into a supervised fine-tuning stage with labeled protein-ligand complexes, as illustrated in Figure 5j. During this phase, the pretrained encoder becomes instrumental, transforming the foremost embedded vector into a crucial latent feature for guiding various downstream tasks. Moreover, to balance the potential biases of a singular modeling approach, sequence-based models are also integrated into the framework. The final output of PLFormer thus emerges as an integrated ensemble of these diverse predictions. Further details on the consensus methodology employed will be elaborated in the forthcoming task-specific results section. Overall, PLFormer stands as a comprehensive framework in protein-ligand interaction analysis, synergizing topological understanding with advanced deep learning techniques. The PLFormer’s detailed settings are available in the Supplementary Information Section SA.2.

Self-supervised and supervised learning in PLFormer. The training of PLFormer model unfolds in two phases: initially, a self-supervised learning phase utilizing unlabeled data for pre-training, and subsequently, supervised learning focusing on specific benchmarks for various tasks, which results in a finely tuned model. Firstly, we collected 19,513 unlabeled protein-ligand complexes from the PDBbind database for the pre-training of the PLFormer model. We reconstructed the path topological embeddings from these complexes to calculate reconstruction loss, using mean square error (MAE) as the metric for this purpose. This self-supervised learning method allows the model to develop profound, generalized representations of protein-ligand complex patterns from a substantial volume of unlabeled data, potentially streamlining the subsequent fine-tuning process. In this study, using approximately 20,000 unlabeled complexes led to exceptional performance in most tasks. Going forward, our goal is to further enrich the pre-training process by including a larger pool of protein-ligand complexes, thereby bypassing the need for experimental data. Specifically for this research, the model’s fine-tuning was centered on the task of binding affinity prediction for

the CASF-2007, CASF-2013, and CASF-2016 benchmarks, using a version of the model fine-tuned on the PDBbind-v2020 dataset. For subsequent 5-fold cross-validation tasks on the SARS-CoV(-2) BA dataset, the prediction model was further refined based on the PDBbind-v2020 fine-tuned model. Throughout these downstream tasks, mean square error was consistently chosen as the loss function, ensuring the model’s focus on reducing the error in its predictions.

Data availability

This study utilized a pre-training dataset that encompasses a collection of protein-ligand complexes sourced from various PDBbind databases, including CASF-2007, CASF-2013, CASF-2016, and PDBbind v2020. To ensure the dataset’s reliability and eliminate redundancies, a meticulous curation process was undertaken, resulting in a total of 19,513 non-overlapping complexes. For scoring, the study used the general set from PDBbind v2020, comprising 19,443 complexes. Excluding core sets from CASF-2007, CASF-2013, CASF-2016, and PDBbind v2016, the final training set for the PLFormer model consisted of 18,904 complexes. All the above-mentioned data can be downloaded from the official PDBbind website: <http://www.pdbbind.org.cn/index.php>. The sequence-based features used in this work derived from the Transformer-CPZ model [28] and the ESM model [27]. These features are readily available for download at <https://github.com/WeilabMSU/PLFormer>. Furthermore, this study includes 155 extra inhibitors of SARS-CoV(-2) BA [37], obtained by excluding overlapping complexes from PDBbind-v2020. These inhibitors, along with 400 single-site mutated proteins (which include the original SARS-CoV-2 main protease, PDBID: 7VH8), are available for download at the following link: <https://github.com/WeilabMSU/PLFormer>.

Code availability

All source codes and models are publicly available at <https://github.com/WeilabMSU/PLFormer>

Acknowledgments

This work was supported in part by NIH grants R01GM126189, R01AI164266, and R35GM148196, National Science Foundation grants DMS2052983 and IIS-1900473, Michigan State University Research Foundation, and Bristol-Myers Squibb 65109.

Ethics declarations

Competing interests

The authors declare no competing interests.

A Supplementary Information

This document provides additional details not essential to the main body of the paper but potentially of interest to readers.

A.1 Evaluation metrics

Evaluation of scoring power. In this research, the evaluation of the models’ prediction accuracy utilizes the Pearson Correlation Coefficient (PCC), which is defined as follows:

$$\text{PCC} = \frac{\sum (x_i - \bar{x})(y_i - \bar{y})}{\sqrt{\sum (x_i - \bar{x})^2 \sum (y_i - \bar{y})^2}} \quad (11)$$

Here, x_i represents the value of the variable x in the i th sample, while \bar{x} denotes the average of the x variable values. Similarly, y_i is the value of the variable y in the i th sample, and \bar{y} is the mean of the y variable values. The Pearson Correlation Coefficient (PCC) is used to describe the relationship between the variables x and y .

The root mean squared error (RMSE) is defined as below:

$$\text{RMSE} = \sqrt{\frac{1}{n} \sum_{i=1}^n (y_i - \hat{y}_i)^2} \quad (12)$$

Here, y_i and \hat{y}_i are predicted value and true value of i th sample respectively.

Loss function for training. In this study, the Mean Squared Error (MSE) is utilized as the loss function throughout both the pre-training and fine-tuning phases. MSE is a commonly employed metric in statistical modeling and machine learning, serving to quantify the discrepancies between predicted values and actual observations. It calculates the average of the squares of the differences between predicted and actual values. The mathematical formulation of MSE is as follows:

$$\text{MSE} = \frac{1}{n} \sum_{i=1}^n (y_i - \hat{y}_i)^2 \quad (13)$$

Here, y_i is the actual value for the i -th data point. \hat{y}_i is the predicted value for the i -th data point. And n is the total number of data points.

A.2 Hyperparameter selection and optimization

In the Seq-ML model, protein and ligand features are initially extracted using Seq-ML Transformers. Following this, the Gradient Boosted Decision Trees (GBDT) algorithm is employed for the prediction of protein-ligand binding affinity. The parameters for the GBDT algorithm are configured as follows: ‘n_estimators’ is set to 10,000, ‘max_depth’ to 7, ‘min_samples_split’ to 2, accompanied by a subsample size of 0.4, and a learning rate of 0.005. All other parameters are maintained at their default settings as specified in the algorithm [56].

In the PLFormer models, a self-supervised learning method is adopted during the pre-training phase, which is then followed by a supervised learning approach in the fine-tuning stage. Additionally, similar to the MAE model [57] in computer vision, PLFormer employs an asymmetric design

in its encoder and decoder. Detailed information about the relevant parameters can be found in Table 4.

Table 4: The parameter settings for PLFormer

Parameters	Pre-training stage	Finetuning stage
attention_probs_dropout_prob	0.1	0.1
decoder_hidden_size	768	/
decoder_intermediate_size	3072	/
decoder_num_attention_heads	12	/
decoder_num_hidden_layers	8	/
hidden_act	gelu	gelu
hidden_dropout_prob	0.1	0.1
hidden_size	1024	1024
image_size(large)	(100, 143)	(100, 143)
image_size(small)	(50, 143)	(50, 143)
initializer_range	0.02	0.02
intermediate_size	4096	4096
num_attention_heads	4096	4096
num_channels	6	6
num_hidden_layers	12	12
patch_size	(1, 143)	(1, 143)

In the pre-training phase of our proposed model, we carefully selected training hyperparameters to foster effective learning and convergence. We employed a batch size of 64 and a limit of 30,000 training steps, along with an initial learning rate of 0.001 to facilitate gradual and effective weight adjustments. To stabilize the early training phase, we incorporated a warm-up period accounting for 5% of the total training steps, where the learning rate gradually increased from 0 to the initial rate. In the subsequent fine-tuning stage, we employed a supervised learning method to refine the model for specific tasks, focusing on preventing overfitting to the hyperparameters. We decreased the batch size to 32 and modified the initial learning rate to 0.0008. The training steps varied for different tasks, setting a maximum of 10,000 steps for the PDBbind v2020 datasets. For the SARS-CoV-2 BA dataset’s 5-fold cross-validation task, we divided the dataset into five parts, training five separate models. Each model was trained using four out of the five dataset parts, building on the model already fine-tuned with PDBbind v2020. These models underwent 4,000 update steps, with a batch size of 8 and a learning rate of 0.0008. It is crucial to note that some parameters, such as warm-up steps and the optimizer, were consistent throughout the pre-training and fine-tuning stages. This consistency supported a cohesive approach in model development. Moreover, during fine-tuning for binding affinity prediction, we consciously limited hyperparameter tuning. This approach not only aids in avoiding overfitting but also ensures the effectiveness of mutation scanning.

A.3 Topological objects

Graph. The graph is a key structure for illustrating relationships among different entities, representing one of the most prevalent data forms. It is composed of nodes (or vertices) and edges, which establish the connections between these nodes. Graphs can be enhanced in several ways, such as by adding directionality to create directed graphs (digraph), assigning weights for weighted graphs, or incorporating geometric properties in geometric graphs. These enhanced graphs are excellent for representing relationships and attributes in various scenarios. Formally, a graph is defined as a pair (V, E) , where V represents a set of vertices and E , a subset of $V \times V$, signifies the set of edges. Vertices and edges are the core components of a graph. Tools like adjacency matrices, degree matrices, and Laplacian matrices are utilized to describe the interactions between vertices and edges. These matrices are pivotal in graph theory and network analysis, capturing the graph's underlying topological structure. Although graphs are inherently one-dimensional, methods from simplicial complexes are sometimes used to express the graph's higher-dimensional aspects. Topological objects include the clique complex, cell complex, cellular sheaf, hypergraph, neighborhood complex, and Hom complex [58, 59].

Simplicial complex. A simplicial complex is a type of topological space constructed from basic units known as simplices. A simplex extends the notion of a triangle or tetrahedron to any number of dimensions. For a set of vertices V , a k -simplex σ_k is typically represented by a subset of V containing $k + 1$ elements, and is expressed as $\sigma = \langle v_0, v_1, \dots, v_k \rangle$. Any subset of σ_{k-1} is considered a face of σ_k .

A *simplicial complex*, denoted as K , based on a vertex set V , is defined by a group of simplices that meet two criteria: (1) If a simplex σ is part of K , then all of its faces, including individual vertices, are also included in K ; (2) The intersection of any two simplices within K is either empty or a face (subset) common to both simplices. From these characteristics, it's evident that a graph can be interpreted as a 1-dimensional simplicial complex, where its simplices consist of vertices (0-simplices) and edges (1-simplices).

In a k -simplex, the boundary is the set of its $(k - 1)$ -dimensional faces. The *boundary operator*, symbolized as ∂_k , operates on a k -simplex $\langle v_0, v_1, \dots, v_k \rangle$ in the following mathematical form:

$$\partial_k \langle v_0, v_1, \dots, v_k \rangle = \sum_{i=0}^k (-1)^i \langle v_0, \dots, \widehat{v}_i, \dots, v_k \rangle, \quad (14)$$

where \widehat{v}_i indicates the exclusion of the vertex v_i . A chain complex is a series of Abelian groups (or modules), interconnected by boundary operators. Suppose G is an Abelian group. The k -th group in the chain complex, denoted as $C_k(K; G)$, comprises formal sums of k -simplices. The boundary operator $\partial_k : C_k(K; G) \rightarrow C_{k-1}(K; G)$ maps a k -simplex to its $(k - 1)$ -dimensional boundary. The sequence of the chain complex can be represented as:

$$\dots \xrightarrow{\partial_{k+1}} C_k(K; G) \xrightarrow{\partial_k} C_{k-1}(K; G) \xrightarrow{\partial_{k-1}} \dots \xrightarrow{\partial_2} C_1(K; G) \xrightarrow{\partial_1} C_0(K; G). \quad (15)$$

A critical characteristic of the boundary operator is that the composition of two consecutive boundary operators equals zero, i.e., $\partial_{k-1} \circ \partial_k = 0$. This implies that the boundary of a boundary is always null, carrying significant topological implications. The structure of the chain complex provides a systematic way to analyze how boundaries integrate with each other.

While simplicial complexes are valuable topological tools for representing relationships in various data, they can be limiting in certain contexts. For these situations, path complex, as a more expansive model and combinatorial structure, offer increased utility in diverse applications.

Path complex. A path complex can be thought of as a way to extend the concept of a graph or a simplicial complex to include paths, which are sequences of vertices in a certain order. Mathematically, let V be a non-empty, finite set. For any non-negative integer p , an *elementary p -path* on V is defined as a sequence $i_0 i_1 \dots i_p$ consisting of elements from V . Notably, when $V = \{0, 1\}$, the collection of elementary paths is uncountable and parallels the set of binary numbers. Let \mathbb{K} represent a field, and let $\Lambda_p = \Lambda_p(V)$ be the \mathbb{K} -vector space generated by all elementary p -paths. To elaborate, for the elementary p -path $i_0 i_1 \dots i_p$, we denote its corresponding generator as $e_{i_0 i_1 \dots i_p}$. The set $\{e_{i_0 i_1 \dots i_p}, i_0, i_1, \dots, i_p \in V\}$ forms a basis for Λ_p over \mathbb{K} . It is established as a convention that $\Lambda_{-1} = 0$, representing the zero space. Any element within Λ_p is referred to as a *p -path*. Therefore, each p -path v can be expressed as

$$v = \sum_{i_0, i_1, \dots, i_p \in V} a^{i_0 i_1 \dots i_p} e_{i_0 i_1 \dots i_p}, \quad \text{where } a^{i_0 i_1 \dots i_p} \in \mathbb{K}.$$

For any integer $p \geq 0$, there exists a \mathbb{K} -linear map $\partial : \Lambda_p \rightarrow \Lambda_{p-1}$. This map is defined as $\partial e_{i_0} = 0$ for $e_{i_0} \in \Lambda_0$ and $\partial e_{i_0 i_1 \dots i_p} = \sum_{k=0}^p (-1)^k e_{i_0 \dots \widehat{i}_k \dots i_p}$ for $p \geq 1$, where \widehat{i}_k denotes the exclusion of the index i_k . It can be shown through direct verification that ∂ functions as a boundary operator on the sequence $(\Lambda_p)_p$, satisfying the condition $\partial^2 = 0$.

A *path complex* on a non-empty finite set V is defined as a non-empty set \mathcal{P} consisting of elementary paths on V . This set has the property that if an elementary path $i_0 i_1 \dots i_p$ is in \mathcal{P} , then both the subsequences $i_0 i_1 \dots i_{p-1}$ and $i_1 i_2 \dots i_p$ are also included in \mathcal{P} . Consider two path complexes, (\mathcal{P}, V) and (\mathcal{Q}, W) . A *morphism of path complexes* is a function $\theta : \mathcal{P} \rightarrow \mathcal{Q}$ that is derived from a mapping between the finite sets V and W . It should be noted that a simplicial complex qualifies as a special case of a path complex. The set of paths (directed edges) on a digraph G is a path complex, denoted by $\mathcal{P}(G)$. And the paths in \mathcal{P} are called *allowed paths*. It can be expressed as

$$\mathcal{A}_p = \mathcal{A}_p(\mathcal{P}) = \left\{ \sum_{i_0, i_1, \dots, i_p \in V} a^{i_0 i_1 \dots i_p} e_{i_0 i_1 \dots i_p} \mid i_0 i_1 \dots i_p \in \mathcal{P}, a^{i_0 i_1 \dots i_p} \in \mathbb{K} \right\}. \quad (16)$$

We adopt the convention that $\mathcal{A}_{-1} = 0$ represents the null space. The set of ∂ -invariant p -paths is defined as

$$\Omega_{-1} = 0, \quad \Omega_p = \Omega_p(\mathcal{P}) = \{x \in \mathcal{A}_p \mid \partial x \in \mathcal{A}_{p-1}\}, \quad \text{for } p \geq 0. \quad (17)$$

Under this definition, the sequence $(\Omega_p)_p$ forms a subchain complex within the larger structure of $(\Lambda_p(V))_p$.

Path complexes can be particularly useful in areas like computational topology, where they are used to study data that can be represented as a network or a graph, such as social networks, biological networks, and sensor networks. They provide a way to generalize the concept of a graph to capture not just relationships between individual elements, but also more complex relationships involving sequences of elements.

A.4 Vietoris-Rips path complex and alpha path complex

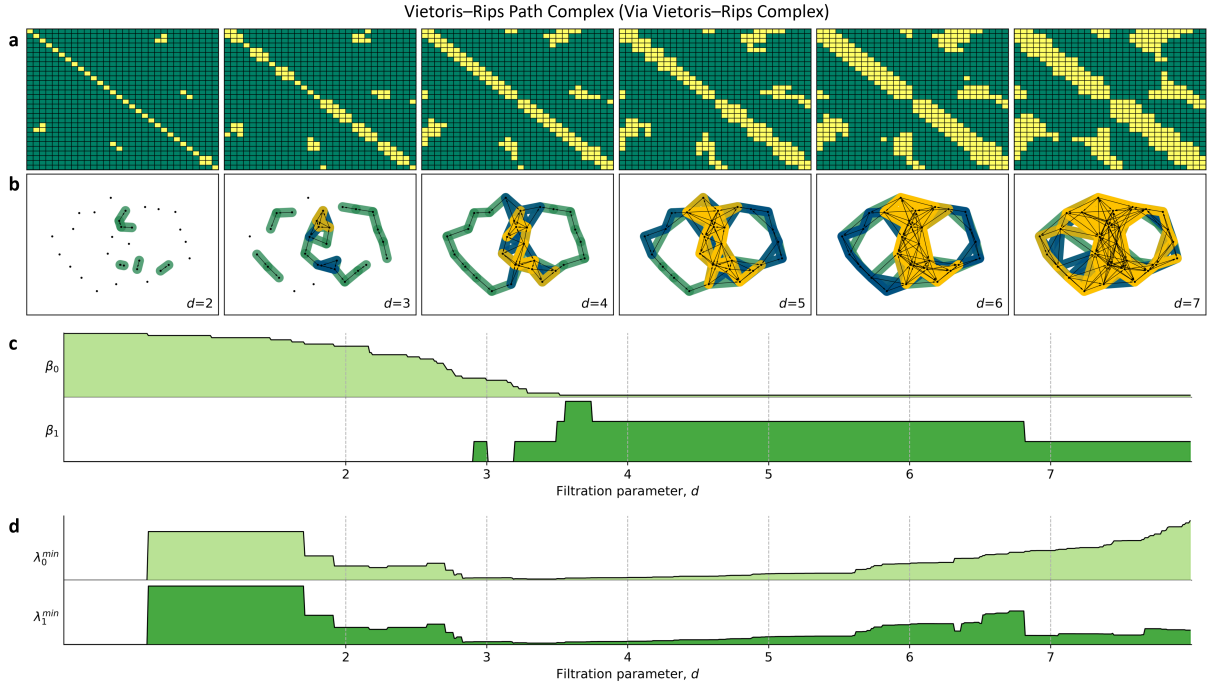


Figure 6: Illustration of Vietoris-Rips path complex across various scales for the point cloud shown in Figure 5a. **a** This part illustrates the adjacency matrices of the point cloud at different scales, characterized by the filtration parameter d . In these matrices, yellow entries signify connections between points where the distance is less than the chosen threshold, whereas green entries mark points that are not connected. **b** The Vietoris-Rips path complexes constructed at multiple scales are displayed, for values of d including 2, 3, 4, 5, 6, and 7. **c** A display of the persistent Betti numbers, labeled as β_i for $i = 0$ and $i = 1$. The specific scales at which these Betti numbers occur are indicated by vertical dashed lines. **d** The non-zero minimum non-harmonic spectra of the persistent path Laplacian in both the 0th and 1st dimensions (λ_0^{\min} and λ_1^{\min}), emphasizing how these values vary with the scale parameter d .

The Vietoris-Rips (VR) path complex presented in this study is based on the standard Vietoris-Rips (VR) complex. Consider a metric space (M, d) and a finite set of points X within M . The VR complex \mathcal{VR}_d , for a specific parameter d , is defined as follows:

$$\mathcal{VR}_d = \{S \subseteq X \mid \text{for every pair of points } x, y \text{ in } S, \text{ the distance } d(x, y) \text{ is less than or equal to } d\}. \quad (18)$$

The Vietoris-Rips (VR) complex is traditionally considered an abstract simplicial complex, meaning that a simplex S is viewed purely as a set, without its geometric structure being taken into account. This abstract perspective leads us to explore more generalized structures. By incorporating geometric characteristics such as angles and volumes, or even their applications in fields like biology or materials science, the path complex emerges as a more adaptable topological model. In this approach, each simplex S in the VR complex is endowed with both weight and orientation information. Specifically, for a VR complex \mathcal{VR}_d , there exists a weight function $w : \mathcal{VR}_d \rightarrow \mathbb{R}$, along with a graded orientation function $\varrho_n : (\mathcal{VR}_d)_n \rightarrow S_{n+1}$ for $n \geq 1$, where S_n represents the permutation group of n elements. Then, for any value $\eta \in \mathbb{R}$, the Vietoris-Rips path complex is

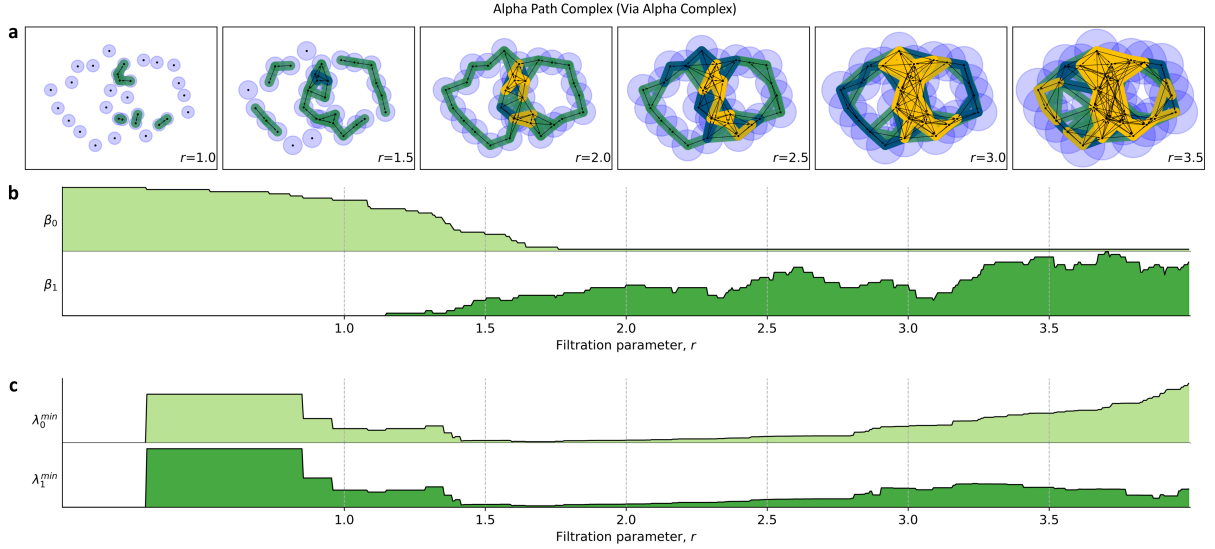


Figure 7: Illustration of the construction of alpha path complex via alpha complex with changing scale parameter for the point cloud in Figure 5a. **a** The constructed alpha path complexes for given scale parameter, i.e., $r = 1.0$, $r = 1.5$, $d = 2.0$, $d = 2.5$, $d = 3.0$, and $d = 3.5$. **c** The persistent Betti numbers of alpha path complexes, $\beta_i, i = 0, 1$. The vertical dash lines indicate the Betti numbers for given scale (filtration) parameters. **d** Representation of nonzero minimum non-harmonic spectra of the persistent path Laplacian at the 0th and 1st dimensions (λ_0^{min} and λ_1^{min}) for alpha path complex, highlighting their dependence on the filtration (scale) parameter d .

mathematically defined as follows:

$$\mathcal{VR}_d\mathcal{P}_\eta := \{S \times \varrho_*(S) | w(S) \leq \eta, S \in \mathcal{VR}_d\}. \quad (19)$$

Thus the element $S \times \varrho_*(S)$ is interpreted as a sequence. By computing the homology and Laplacians of path complexes, we can uncover topological and geometric features of a point set. For this study, we define the weight function $w : \mathcal{VR}_d \rightarrow \mathbb{R}$ and the graded orientation function $\varrho_n : (\mathcal{VR}_d)_n \rightarrow S_{n+1}$ as trivial functions. This simplifies the path complex construction, aligning it closely with the Vietoris-Rips complex.

Informally, a Vietoris-Rips (VR) complex is a simplicial complex formed by finite sets of points where every two points in a set are within a certain maximum distance, defined by the filtration parameter. Building upon this, path complexes are developed on all simplices of the complex. This step involves incorporating geometric details of the simplices, considering both their orientation and size. By selecting specific simplices and assigning them orientations, we create a group of chosen simplices, forming a path complex. When the orientation for each path complex follows a pre-established order of points, the resulting path complex is seen as a subset within the array of these path complexes. Under these conditions, the VR path complex can be simplified to a hypergraph structure. Furthermore, if we ignore the size aspect of the simplices, effectively choosing all simplices, the VR path complex then aligns with the VR complex itself. In such instances, we refer to the VR path complex as $\mathcal{VRP}_d(X)$.

The VR path complex $\mathcal{VRP}_d(X)$ effectively represents the topological characteristics of the underlying space, with the scale of observation defined by the parameter d . As depicted in Figure 6a and b, with an increase in d , additional simplices are included, leading to the formation of

a greater number of paths. This enrichment in the complex’s structure offers insights into the connectivity and the presence of voids within the space across varying scales.

Likewise, the alpha path complex can be formed based on the alpha complex. In a metric space (M, d) with a finite set of points X in M , the alpha complex \mathcal{A}_r is defined, for a given parameter r , as

$$\mathcal{A}_r = \{S \subseteq X \mid \text{there exists a disk with radius } r \text{ encompassing } S\}. \quad (20)$$

Commonly, the alpha complex is viewed as an abstract simplicial complex, primarily for computing its homology. Nonetheless, the alpha complex inherently has a geometric structure. By considering functions $w : \mathcal{A}_r \rightarrow \mathbb{R}$ and $\varrho_n : (\mathcal{A}_r)_n \rightarrow S_{n+1}$, for any real number η , the alpha path complex can be derived:

$$\mathcal{A}_r \mathcal{P}_\eta = \{S \times \varrho_*(S) \mid w(S) \leq \eta, S \in \mathcal{A}_r\}. \quad (21)$$

Analogous to the correlation between the alpha complex and the VR complex, alpha path complexes can reveal different types of information compared to VR path complexes. If the mappings $w : \mathcal{A}_r \rightarrow \mathbb{R}$ and $\varrho_n : (\mathcal{A}_r)_n \rightarrow S_{n+1}$ are selected as trivial functions, then the alpha path complex can be simplified to align with the alpha complex.

Put simply, the alpha complex consists of simplices that are sufficiently close together, such that a disk of a specified radius encompasses all the points in a simplex. This structure can also be conceptualized from the perspectives of the 3-dimensional Voronoi diagram [60] or the Delaunay triangulation [61]. The alpha path complex, on the other hand, comprises simplices within the alpha complex, each assigned a corresponding orientation. If this orientation follows a predetermined sequence, the alpha path complex can be simplified to form a hypergraph. Additionally, if all simplices of the alpha complex are selected, the alpha path complex essentially becomes equivalent to the alpha complex itself. In this particular scenario, the formation is denoted by $\mathcal{A}_r \mathcal{H}(X)$.

For a specified parameter $r > 0$, the construction of the alpha complex and the alpha path complex, represented as $\mathcal{A}_r(X)$ and $\mathcal{A}_r \mathcal{H}(X)$ respectively, proceeds in the following stages: 1. Introduce a vertex for every point in the set X . 2. For any subset S within X , where the greatest pairwise distance among points in S does not exceed r , incorporate a simplex into the complex. The vertices of this simplex correspond to the points in S . 3. Define paths on all the simplices based on the pre-established sequence of the set X , and then construct the path complex $\mathcal{A}_r \mathcal{H}(X)$ as the aggregate of these paths.

The alpha path complex incorporates paths for point subsets that are within a given radius, indicating close proximity. With an increase in the parameter r , more paths are integrated into the path complex, as depicted in Figure 7a. This addition of paths reveals various degrees of connectivity and different features within the dataset. Figures 6c, d and 7b, c demonstrate that, while the higher-dimensional persistent attributes of VR path Laplacians and alpha path Laplacians show significant differences, the 0-dimensional persistent patterns of both remain consistent. Figures 6 and 7 showcase the formation of the VR path complex and the alpha path complex, respectively, under various filtration parameters. It is important to note that both path complexes in this research are constructed on the basis of the simplicial complex, incorporating elements from both the Vietoris-Rips (VR) complex and the alpha complex.

A.5 Element-specific topology

Unlike differential geometry, which has localized operators, topology is global in the sense that topological invariants of a point cloud provide information for the collective cloud. However, we often need localized "topological information" for each point in the cloud or certain types of elements. To this end, atom-specific persistent homology [62] and element-specific persistent homology [63] were proposed. These methods achieve better localization and can be used to embed local information into topological invariants. In particular, atom-specific and element-specific topologies enable the embedding of physical, chemical, and biological information, such as covalent bonds, hydrogen bonds, and polar, nonpolar, van der Waals, and hydrophobic interactions in topological invariants. For example, the multiscale topological invariants extracted from the nitrogen element are expected to reveal hydrogen bond strength, while those from the carbon element will be associated with hydrophobic interactions.

In addition to atom-specific and element-specific topologies, persistent co-homology was also developed for the same purpose [64]. This approach allows us to effectively deal with multicomponent heterogeneous information, such as geometry and electrostatics. More recently, persistent sheaf Laplacians have been proposed as a more elegant topological tool to achieve localization [65]. The element-specific persistent path Laplacians developed in this work follow the same principle.

A.6 PLFormer components

In the method section, we introduced the novel Path Topological Sequence Embedding module, a key innovation in our PLFormer model that significantly enhances its capability to capture complex data relationships. In this section, we aim to elucidate the remaining components of PLFormer, which closely align with the architecture of the Masked Autoencoder (MAE) [57], as shown in Figure 5i and j. Our model inherits MAE’s robust framework for efficient and effective feature learning, particularly its encoder-decoder structure optimized for handling high-dimensional data. We will detail how each component of PLFormer. This comprehensive overview will provide a deeper understanding of PLFormer’s architecture.

PLFormer Encoder. The Path Topological Sequence Embedding, once fed into the system, initially passes through a convolution layer. This step is crucial for downsampling the topological embedding, optimizing it for subsequent processing by the encoder modules. Following this convolution layer, the processed embedding advances to multiple encoder layers. These layers are the same as the architecture of the Transformer Encoder, each comprising two primary components: (1) a Multi-Head Self-Attention (MHSA) mechanism and (2) a Feed-Forward Neural Network (FFNN). Both components are augmented by normalization layers and incorporate residual connections to enhance the flow of information and learning stability.

For the MHSA, the key mechanism used is the ‘Scaled Dot-Product Attention’. The input to this mechanism consists of queries (Q), keys (K), and values (V), which are all vectors. The attention mechanism is defined as:

$$\text{Attention}(Q, K, V) = \text{softmax}\left(\frac{QK^T}{\sqrt{d_k}}\right)V \quad (22)$$

Here, d_k is the dimension of the key vectors. This scaling factor ($\sqrt{d_k}$) is crucial as it prevents the dot products from growing too large in magnitude, leading to smoother gradients. Specifically, within the framework of PLFormer, each scale’s Path Topological Embedding is adeptly transformed into three distinct vectors: queries (Q), keys (K), and values (V). This transformation is achieved through separate linear transformations, each governed by learnable weights. Subsequently, the attention mechanism is applied across the entire sequence. This process enables each element in the sequence to dynamically attend to every other element, fostering a comprehensive inter-element relationship analysis. Additionally, the Transformer architecture in PLFormer is designed to utilize multiple attention heads, further enhancing its capability to capture and process complex patterns in the data. Each head learns different aspects of the data:

$$\text{MultiHead}(Q, K, V) = \text{Concat}(\text{head}_1, \text{head}_2, \dots, \text{head}_h)W^O \quad (23)$$

Where each head is defined as:

$$\text{head}_i = \text{Attention}(QW_i^Q, KW_i^K, VW_i^V) \quad (24)$$

Here, W_i^Q , W_i^K , W_i^V , and W^O are parameter matrices. h is the number of heads.

Beyond the attention mechanism, each encoder layer in the model is equipped with a fully connected feed-forward network. This network operates independently and identically on each

scale within the layer. This consists of two linear transformations with a GELU (Gaussian Error Linear Unit) activation in between:

$$\text{FFN}(x) = \max(0, xW_1 + b_1)W_2 + b_2 \quad (25)$$

Here, W_1 , W_2 , b_1 , and b_2 are learnable parameters. The GELU activation function introduces non-linearity.

Each sub-layer (MHSA and FFNN) in the encoder layer is followed by layer normalization and a residual connection. The output of each sub-layer is:

$$\text{Output} = \text{LayerNorm}(x + \text{Sublayer}(x)) \quad (26)$$

Here, x is the input to the sub-layer. $\text{Sublayer}(x)$ is the function implemented by the sub-layer itself (either MHSA and FFNN).

PLFormer Decoder. In this work, the PLFormer adopts an asymmetric design. This design features a more substantial and complex encoder relative to its decoder. The decoder’s primary role in the PLFormer is to reconstruct the original path topological sequence embedding from the latent representations generated by the encoder. This reconstruction process is pivotal, as it compels the decoder to accurately regenerate the path topological sequence, thereby driving the encoder to develop rich and insightful representations of the protein-ligand complex data. Such representations are invaluable for a variety of downstream applications.

Structurally, the layers within the PLFormer Decoder closely mirror those of the PLFormer Encoder. The process begins with the encoder’s latent representations being linearly mapped. These mappings are then input into the PLFormer Decoders, which are architecturally similar to the encoder layers in the PLFormer Encoder, albeit with a reduced hidden size. During the pre-training phase, the output from the final decoder layer undergoes a transformation back into the original path topological sequence, facilitated by a convolution layer. In the fine-tuning stage, the focus shifts to the output derived from the first scale’s hidden state, which is utilized for regression tasks, such as binding affinity prediction. Specifically, this output is channeled through a linear layer, culminating in the generation of the final predictive outputs.

A.7 Supplementary tables

In the following section, we provide supplementary tables that offer additional data and insights pertinent to our study. Readers are encouraged to refer to these tables for a more detailed exploration of the topics covered in the main text.

Table 5: Statistical results of single-point mutation prediction at each interaction site of SARS-CoV-2 M^{pro} , as illustrated in the box plot presented in Figure 3c.

	Mean	Median	Std	First quartile (Q1)	Third quartile (Q3)
H41	-0.105	-0.223	0.291	-0.281	-0.033
M49	-0.116	-0.145	0.081	-0.186	-0.036
Y54	-0.118	-0.124	0.053	-0.135	-0.114
F140	-0.107	-0.154	0.132	-0.188	-0.065
L141	-0.155	-0.145	0.062	-0.164	-0.137
N142	-0.185	-0.191	0.054	-0.219	-0.166
G143	-0.133	-0.139	0.049	-0.155	-0.1
S144	-0.092	-0.105	0.109	-0.152	-0.046
C145	-0.652	-0.648	0.231	-0.808	-0.55
H163	-0.158	-0.209	0.16	-0.267	-0.016
H164	-0.168	-0.173	0.049	-0.198	-0.147
M165	-0.219	-0.38	0.381	-0.472	-0.085
E166	0.105	0.035	0.241	-0.075	0.175
L167	-0.163	-0.136	0.141	-0.258	-0.084
P168	-0.109	-0.114	0.033	-0.136	-0.096
H172	-0.07	-0.039	0.132	-0.187	-0.003
D187	-0.099	-0.144	0.253	-0.194	-0.068
R188	-0.185	-0.129	0.217	-0.153	-0.099
Q189	-0.106	-0.118	0.059	-0.139	-0.066
T190	-0.118	-0.119	0.048	-0.158	-0.08
Q192	-0.048	0.025	0.184	-0.053	0.066

Table 6: Statistical results of single-point mutation prediction at each interaction site of SARS-CoV-2 M^{Pro} , as illustrated in the box plot presented in Figure 3d. ‘Mean of Positive’ represents the average of all mutations that resulted in a positive affinity change, while ‘Mean of Negative’ refers to the average energy difference of mutations that had a negative impact at each sites.

	Maximum	Minimum	Mean of Positive	Mean for Negative
H41	0.754	-0.448	0.305	-0.241
M49	0.016	-0.219	0.008	-0.13
Y54	0.032	-0.242	0.016	-0.133
F140	0.277	-0.265	0.157	-0.154
L141	0.0	-0.361	0.0	-0.163
N142	0.0	-0.263	0.0	-0.195
G143	0.0	-0.242	0.0	-0.14
S144	0.114	-0.383	0.071	-0.133
C145	0.0	-1.132	0.0	-0.686
H163	0.176	-0.353	0.085	-0.239
H164	0.0	-0.238	0.0	-0.177
M165	0.958	-0.592	0.414	-0.377
E166	0.82	-0.195	0.21	-0.091
L167	0.136	-0.488	0.068	-0.189
P168	0.0	-0.143	0.0	-0.115
H172	0.224	-0.244	0.099	-0.126
D187	0.64	-0.528	0.242	-0.213
R188	0.0	-0.824	0.0	-0.195
Q189	0.0	-0.254	0.0	-0.112
T190	0.0	-0.19	0.0	-0.124
Q192	0.083	-0.656	0.052	-0.233

Table 7: The quantitative impact of single-point mutations on binding affinity ($\Delta\Delta G$) for 21 residues surrounding PAXLOVID. Each residue undergoes evaluation for 20 potential mutations, including the original residue where $\Delta\Delta G = 0 = 0$ kcal/mol. The unit of measurement is kcal/mol.

	A	R	N	D	C	Q	E	G	H	I
H41	-0.272	-0.353	-0.408	-0.303	-0.273	-0.448	-0.076	-0.291	0.000	-0.045
M49	-0.176	-0.002	-0.146	-0.190	-0.188	-0.144	-0.175	-0.173	-0.072	-0.020
Y54	-0.114	-0.242	-0.131	-0.132	-0.146	-0.128	-0.143	-0.147	-0.115	-0.126
F140	-0.150	-0.188	-0.157	-0.244	-0.151	-0.201	-0.265	-0.171	-0.049	0.277
L141	-0.161	-0.146	-0.137	-0.208	-0.152	-0.142	-0.143	-0.158	-0.143	-0.193
N142	-0.168	-0.211	0.000	-0.141	-0.143	-0.216	-0.245	-0.181	-0.182	-0.166
G143	-0.134	-0.087	-0.128	-0.242	-0.113	-0.171	-0.163	0.000	-0.100	-0.144
S144	-0.148	-0.112	-0.106	-0.192	-0.062	-0.171	-0.050	-0.140	-0.080	0.114
C145	-0.875	-0.483	-0.710	-0.643	0.000	-0.807	-0.690	-0.520	-0.468	-0.560
H163	-0.262	-0.336	-0.171	-0.195	-0.309	-0.217	-0.282	-0.353	0.000	-0.220
H164	-0.212	-0.144	-0.181	-0.207	-0.238	-0.177	-0.198	-0.167	0.000	-0.148
M165	-0.508	-0.485	-0.452	-0.249	-0.337	-0.451	-0.489	-0.544	-0.592	-0.119
E166	-0.092	0.053	0.035	-0.092	-0.085	-0.074	0.000	0.063	-0.195	0.131
L167	-0.072	-0.268	-0.235	-0.255	-0.010	-0.378	-0.488	-0.098	-0.145	-0.112
P168	-0.115	-0.140	-0.120	-0.064	-0.122	-0.099	-0.090	-0.094	-0.101	-0.140
H172	-0.168	0.160	-0.028	-0.171	-0.193	0.224	-0.033	-0.184	0.000	-0.009
D187	-0.168	-0.528	-0.148	0.000	-0.118	-0.330	-0.371	-0.187	-0.216	0.031
R188	-0.101	0.000	-0.151	-0.134	-0.824	-0.176	-0.082	-0.106	-0.103	-0.143
Q189	-0.153	-0.083	-0.135	-0.102	-0.116	0.000	-0.150	-0.176	-0.071	-0.051
T190	-0.081	-0.059	-0.173	-0.147	-0.105	-0.103	-0.066	-0.190	-0.122	-0.168
Q192	0.047	0.053	-0.121	0.024	0.083	0.000	-0.002	0.074	0.075	0.025
	L	K	M	F	P	S	T	W	Y	V
H41	-0.070	0.163	-0.105	0.138	-0.243	-0.277	-0.247	0.470	0.754	-0.202
M49	-0.078	-0.083	0.000	0.016	-0.218	-0.185	-0.219	-0.012	-0.041	-0.209
Y54	-0.121	-0.133	-0.099	-0.120	-0.113	-0.117	-0.106	0.032	0.000	-0.154
F140	-0.203	-0.160	-0.168	0.000	-0.070	-0.190	-0.036	-0.094	-0.114	0.193
L141	0.000	-0.137	-0.110	-0.174	-0.361	-0.158	-0.136	-0.131	-0.140	-0.171
N142	-0.147	-0.223	-0.166	-0.226	-0.263	-0.225	-0.217	-0.200	-0.173	-0.213
G143	-0.145	-0.152	-0.147	-0.095	-0.170	-0.145	-0.124	-0.087	-0.100	-0.210
S144	-0.120	-0.104	-0.170	-0.164	-0.383	0.000	0.079	-0.033	-0.087	0.093
C145	-0.811	-1.132	-0.843	-0.652	-0.976	-0.403	-0.570	-0.696	-0.609	-0.594
H163	-0.201	0.145	0.043	-0.021	-0.221	-0.335	-0.259	0.176	0.062	-0.200
H164	-0.144	-0.174	-0.199	-0.165	-0.188	-0.226	-0.162	-0.172	-0.109	-0.146
M165	0.367	-0.452	0.000	0.332	-0.422	-0.467	-0.338	-0.017	0.958	-0.108
E166	0.035	-0.019	0.008	0.820	0.267	-0.077	0.151	0.353	0.570	0.248
L167	0.000	-0.223	-0.311	-0.294	0.136	-0.088	-0.060	-0.140	-0.132	-0.097
P168	-0.112	-0.140	-0.143	-0.135	0.000	-0.084	-0.141	-0.096	-0.114	-0.128
H172	-0.194	-0.007	-0.004	-0.230	-0.159	-0.223	-0.044	0.106	-0.244	0.006
D187	-0.091	-0.174	0.113	-0.137	-0.176	-0.138	-0.273	0.425	0.640	-0.141
R188	-0.095	-0.106	-0.160	-0.130	-0.073	-0.821	-0.144	-0.178	-0.127	-0.050
Q189	-0.128	-0.124	-0.125	-0.038	-0.017	-0.159	-0.254	-0.120	-0.040	-0.077
T190	-0.062	-0.162	-0.162	-0.115	-0.156	-0.147	0.000	-0.078	-0.153	-0.113
Q192	0.025	-0.656	-0.227	0.074	-0.231	0.071	-0.360	0.063	0.064	-0.030

A.8 Supplementary figures

In this section, we present a series of supplementary figures that further elucidate and complement the findings discussed in the main text. Readers are encouraged to consult these figures for a richer understanding and visual representation of the concepts and results introduced in the main manuscript.

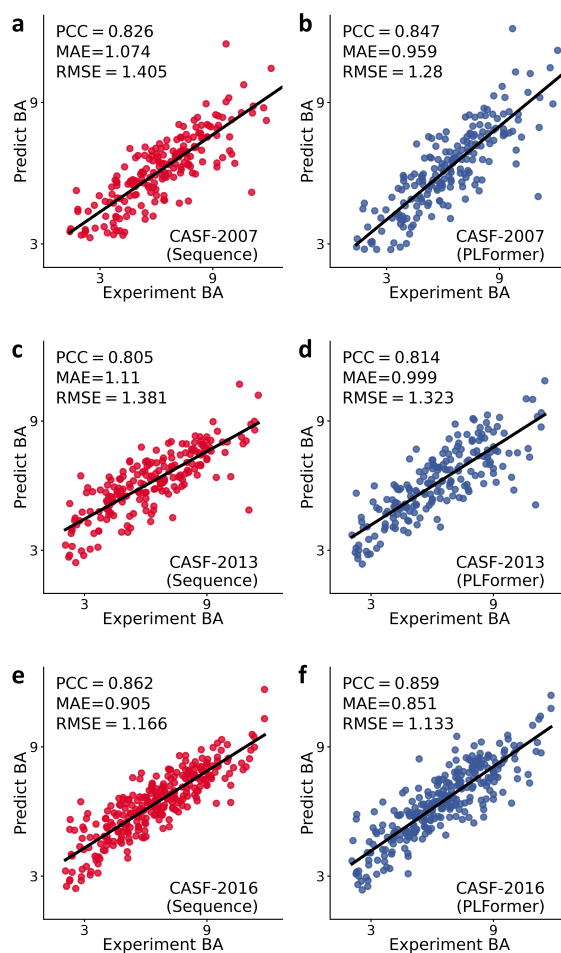


Figure 8: Comparison of PLFormer and Seq-ML models in predicting protein-ligand complex binding affinity. Panels **a** and **b** illustrate the correlation between predicted binding affinities (measured in kcal/mol) by the Seq-ML model (shown in **a**) and the PLFormer model (depicted in **b**), against the experimental results from the CASF-2007 dataset. Panels **c** and **d** display similar correlations for the CASF-2013 dataset. Finally, panels **e** and **f** represent the correlations between predictions and experimental results for the CASF-2016 dataset.

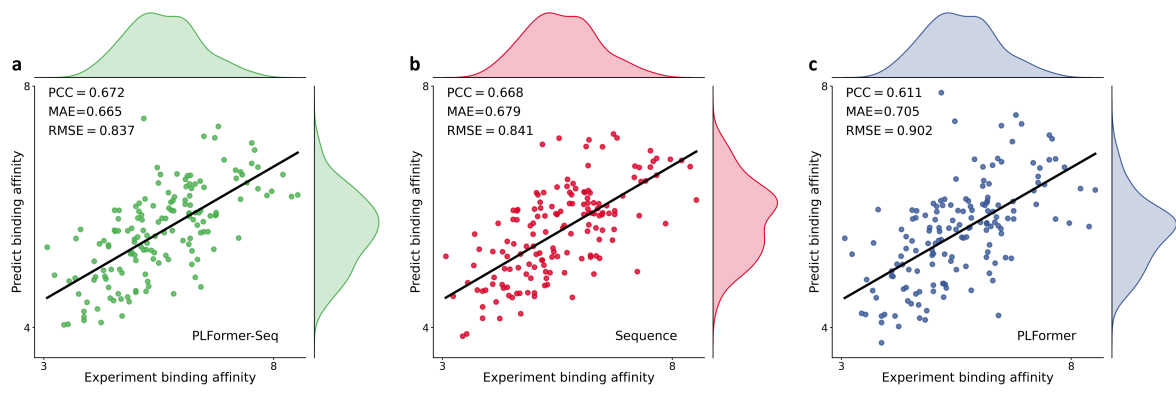


Figure 9: Evaluation of the PLFormer-Seq consensus model (a), PLFormer model (b), and Seq-ML model (c) in predicting protein-ligand complex binding affinity using 5-fold validation for the SARS-CoV-2 BA dataset.

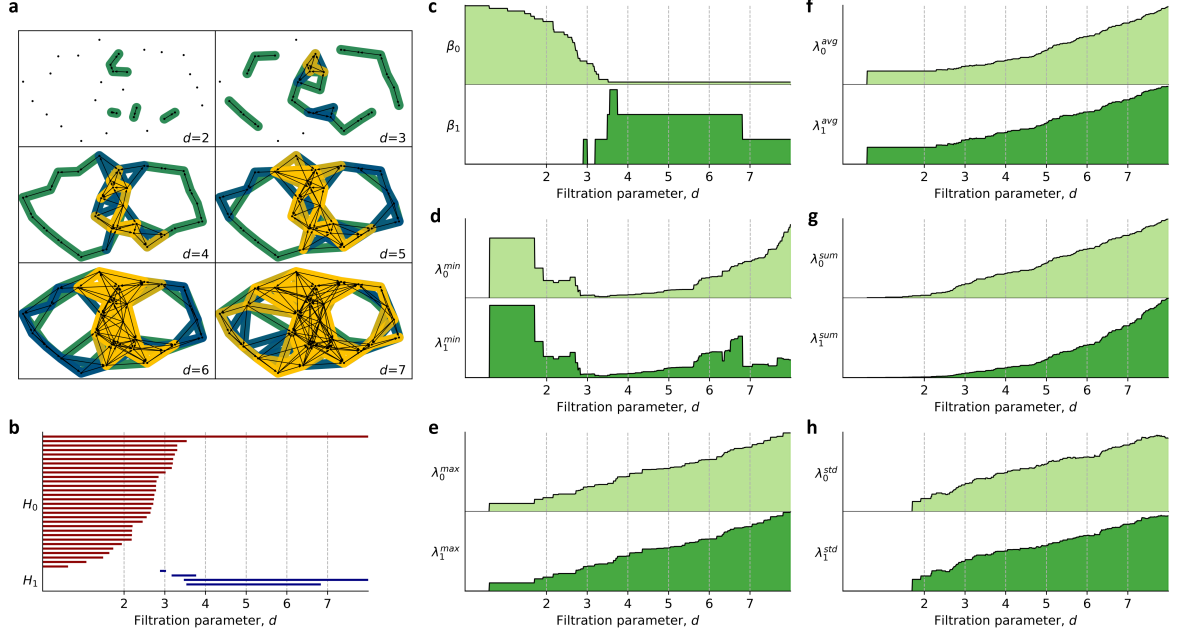


Figure 10: Analysis of persistent path Laplacian versus persistent path homology for the point cloud shown in Figure 5a. **a**, Illustration of the impact of varying the filtration parameter alters the connectivity of the point cloud, leading to a sequence of path complexes that represent different topological structures. **b**, Depicts the barcodes for persistent path homology groups H_0 and H_1 at the 0th and 1st dimensions, respectively, highlighting their changes relative to the filtration parameter d . **c**, Visualization of the variations in the topological invariants at the 0th (β_0) and 1st (β_1) dimensions of the persistent topological path complex, with respect to the filtration (scale) parameter d . **d**, Representation of the nonzero minimum non-harmonic spectra of the persistent path Laplacian at the 0th and 1st dimensions (λ_0^{min} and λ_1^{min}), emphasizing their dependency on the filtration parameter d . **e**, Representation of the maximum non-harmonic spectra of the persistent path Laplacian at the 0th and 1st dimensions (λ_0^{max} and λ_1^{max}), highlighting their reliance on the filtration parameter d . **f**, Displays the average values of nonzero spectra for the persistent path Laplacian in both the 0th and 1st dimensions (λ_0^{avg} and λ_1^{avg}). **g**, Illustrates the standard deviation of nonzero spectra for the persistent path Laplacian in the 0th and 1st dimensions (λ_0^{std} and λ_1^{std}). **h**, Shows the summation of nonzero spectra values for the persistent path Laplacian in the 0th and 1st dimensions (λ_0^{sum} and λ_1^{sum}).

Figure 10 illustrates the persistent characteristics obtained from the non-harmonic spectra of a persistent path Laplacian in both the 0th and 1st dimensions. By incrementally modifying d , a series of hierarchical data representations can be obtained, as depicted in Figure 10a. Figure 10e showcases the progression of zero eigenvalue multiplicities in the corresponding Laplacian matrix as the filtration (scale) parameters evolve, while Figure 10f and g illustrates the changes in the nonzero minimum and maximum positive eigenvalue as the filtration (scale) parameters vary. The standard deviations of the nonzero spectra in these dimensions are denoted by λ_0^{std} and λ_1^{std} , as depicted in Figure 10b. Furthermore, the average values of the nonzero spectra in the 0th and 1st dimensions, labeled as λ_0^{avg} and λ_1^{avg} , are displayed in Figure 10a. The summation values of the nonzero spectra for the persistent path Laplacian, represented by λ_0^{sum} and λ_1^{sum} , are shown in Figure 10c. Additionally, the persistent path homology for the Vietoris-Rips path complex is portrayed in Figure 10d. This part of the figure exhibits the persistent barcodes for homology groups H_0 and H_1 in the 0th and 1st dimensions, respectively. The topological invariants, specifically the Betti numbers, correspond to the frequency of the zero eigenvalue in the path Laplacian for a

specified filtration parameter d . It is important to note that these persistent attributes change with varying filtration parameters, thereby capturing both topological and geometric data in a multiscale fashion.

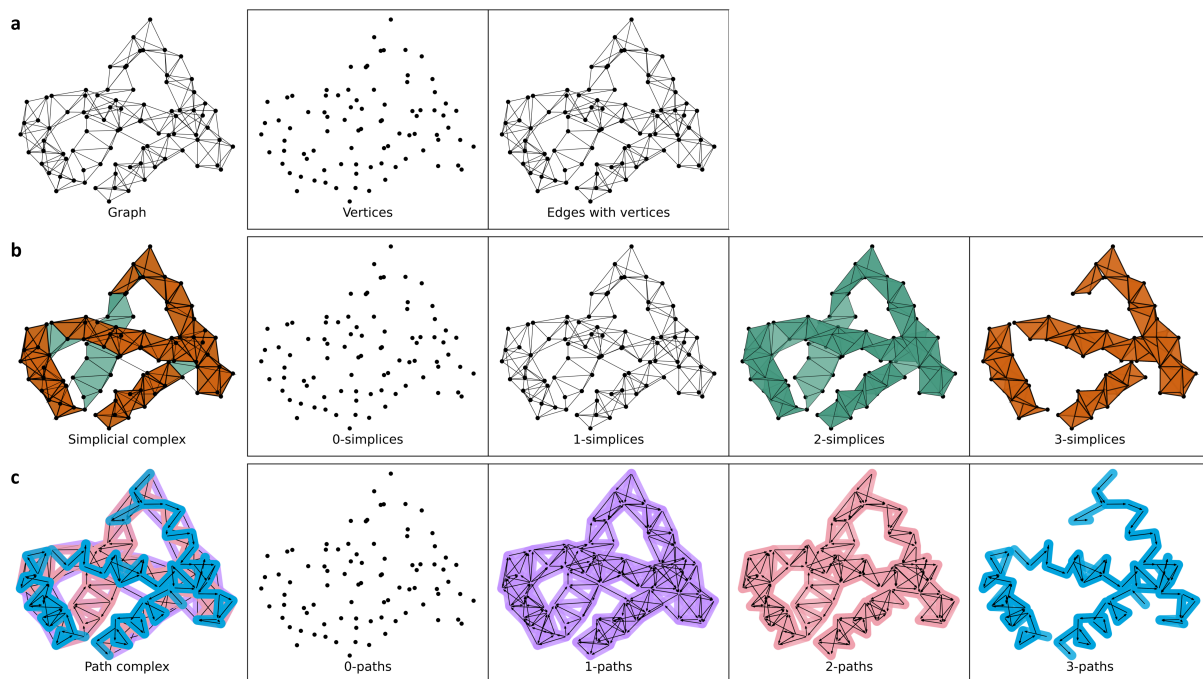


Figure 11: Illustration of different representations for C_{α} atoms in protein (PDBID: IMYL). **a** The graph representation of the structure. **b** The simplicial complex representation of the structure, including a list of 0-simplices, 1-simplices, 2-simplices, and 3-simplices in the complex. **c** The path complex representation of the structure, along with a list of 0, 1, 2, and 3-path within the path complex.

Figure 11 showcases a variety of topological representations for the C_{α} atoms in protein (PDBID: IMYL), using a cutoff distance of 5 Å. In Figure 11a, the traditional graph representation of the protein structure is displayed. Building upon this graph representation, the 0-simplices in the simplicial complex are equivalent to the vertices in the graph, and the 1-simplices correspond to edges connecting these vertices, as demonstrated in the second and third rows of Figures 11a and b. Additionally, higher-dimensional simplices within the simplicial complex reveal more complex aspects of the structure; for instance, 3-simplices can approximate the structure of alpha helices. Moreover, path complexes, with their directional attributes, offer a more comprehensive perspective than simplicial complexes. The path complex representation, incorporating paths of various dimensions, captures multi-level structural information, as depicted in Figure 11c. Notably, the representation through 3-paths can also highlight the presence of an alpha helix.

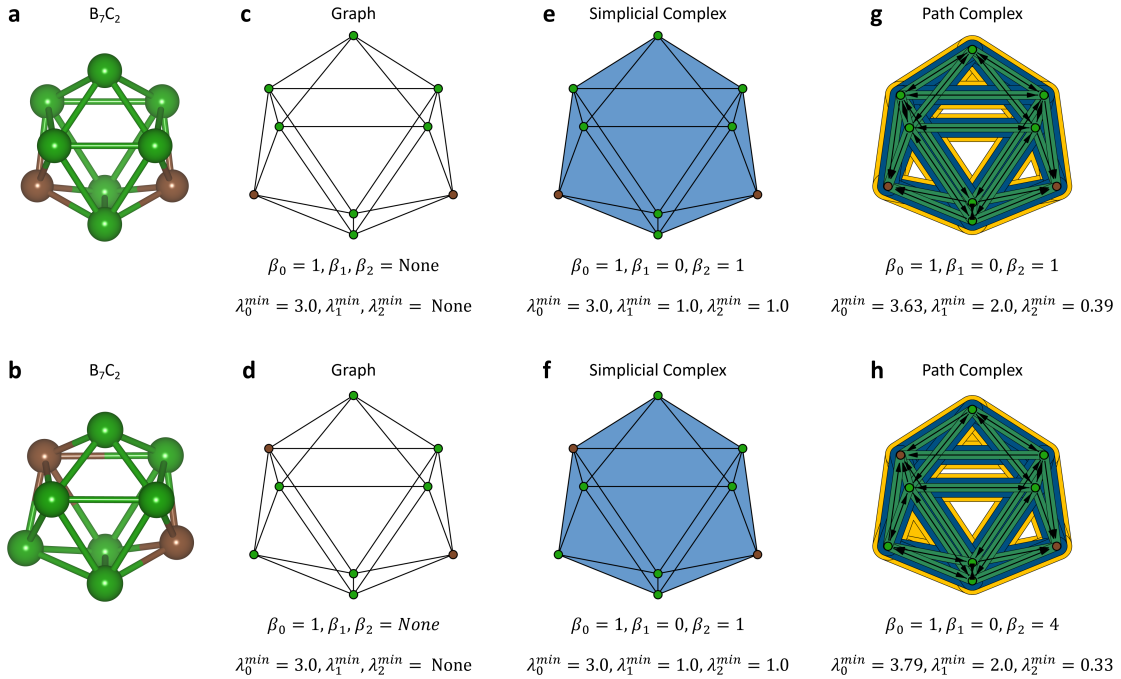


Figure 12: Depiction of diverse Laplacian analyses for two $B_7C_2H_9$ isomers. **a** and **b** Present the structural forms of the two $B_7C_2H_9$ isomers post hydrogen atom removal, with distinctions solely in the placement of carbon atoms. **c** and **d** Showcase the graph structures of **a** and **b**. Here, carbon atoms are emphasized in coffee color, and boron atoms in light green. These graphs contain at most one-dimensional topological information from the Laplacian matrix, e.g., $\beta_0 = 1$ and $\lambda_0^{\min} = 3.0$. **e** and **f** Illustrate the simplicial complex representations of **a** and **b**. Carbon atoms are in coffee color, boron atoms in light green, and 2-simplices shaded light blue. Their topological invariants and non-harmonic spectra align, with $\beta_0 = 1$, $\beta_1 = 0$, and $\beta_2 = 1$, and minimum values $\lambda_0^{\min} = 3.0$, $\lambda_1^{\min} = 1.0$, and $\lambda_2^{\min} = 1.0$. **g** Represents the path complex for structure **b**, noting topological invariants as $\beta_0 = 1$, $\beta_1 = 0$, and $\beta_2 = 4$, and minimum non-zero non-harmonic spectra values $\lambda_0^{\min} = 3.79$, $\lambda_1^{\min} = 2.0$, and $\lambda_2^{\min} = 0.33$. The disparities in figures **g** and **h** highlight the ability of path Laplacians to differentiate these two isomers.

To demonstrate the effectiveness of the proposed path complex and its Laplacian, two $B_7C_2H_9$ isomers with identical geometrical configurations, differing only in the positions of carbon atoms, are employed for validation. In this analysis, we consider the structures excluding hydrogen atoms, as illustrated in Figure 12a and b. Figures 12c, e, and g display the graph, simplicial complex, and path complex representations, along with the results of their respective Laplacian analyses, for the structure shown in 12a. Similarly, Figures 12d, f, and h present these representations and their Laplacians' analysis results for the structure depicted in Figure 12d. Although the structures in 12a and b only differ in the positioning of carbon atoms, the Laplacian analyses for the graph and simplicial complex fail to distinguish between them, with the graph lacking higher-dimensional information. The path complex, however, can encode non-symmetric and non-balanced relations through paths, allowing the shifted positions of carbon atoms to be captured by the path, leading to distinct path Laplacians. Consequently, either the multiplicity of the zero eigenvalue of these Laplacians (β_0 , β_1 , and β_2) or the minimum nonzero spectra of these Laplacians (λ_0^{\min} , λ_1^{\min} , and λ_2^{\min}) can effectively differentiate these two isomeric structures.

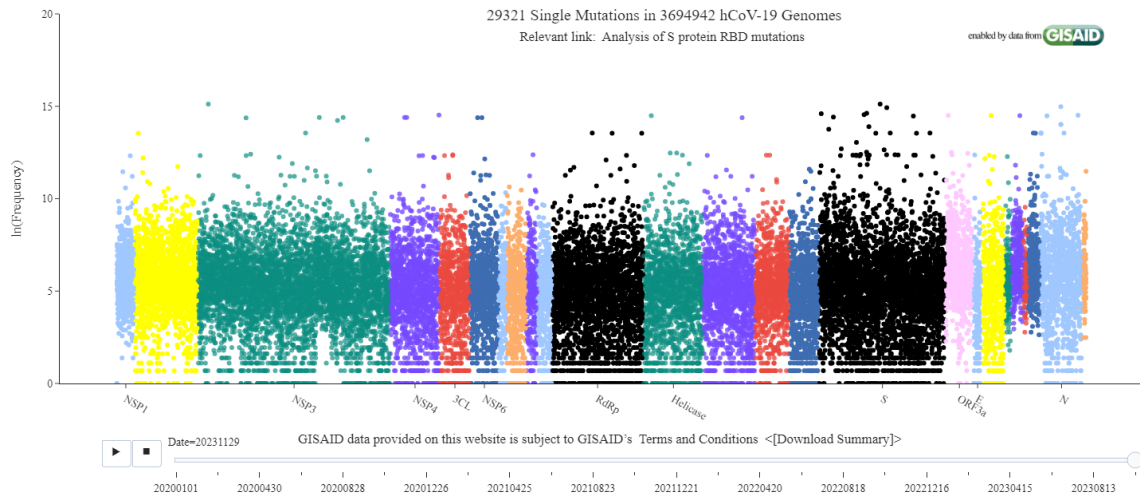


Figure 13: Illustration of the distribution of 29,321 single mutations across 3,694,942 hCoV-19 genomes as of November 29, 2023. The x-axis indicates the nucleotide positions of mutations, starting from position 266, which accounts for the initial gap. Different colors represent various protein domains to facilitate differentiation, with key domains like 3CL and Spike highlighted for clarity. Mutation frequency at each position is calculated by aggregating occurrences, using 'ln(Frequency)' for visualization to evenly represent both high-frequency hotspots and lower-frequency cold spots.

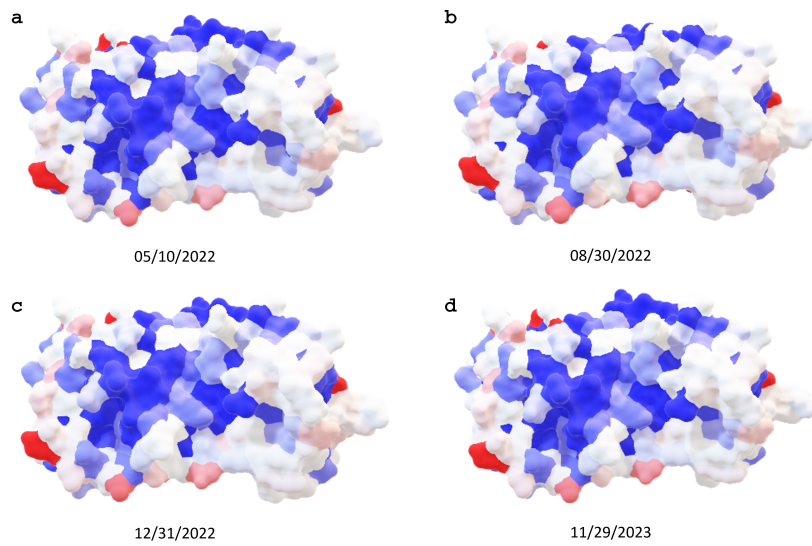


Figure 14: Mutation frequency in SARS-CoV-2 Mpro 3D models for different dates. In this color-coded visualization of a protein surface, blue indicates regions with low mutation frequencies (below 240). The gradient from blue to white for moderate frequencies (between 240 and 500). White regions denote higher mutation frequencies (500 to 5000). Frequencies above 5000 are colored by the gradient from white to red. Mutation frequency up to **a**, 05/10/2022; **b**, 08/30/2022; **c** 12/31/2022; and **d**, 11/29/2023.

References

- [1] Emmanuel Heilmann, Francesco Costacurta, Seyed Arad Moghadasi, Chengjin Ye, Matteo Pavan, Davide Bassani, Andre Volland, Claudia Ascher, Alexander Kurt Hermann Weiss, David Bante, et al. Sars-cov-2 3clpro mutations selected in a vsv-based system confer resistance to nirmatrelvir, ensitrelvir, and gc376. *Science Translational Medicine*, 15(678):eabq7360, 2022.
- [2] Stephen J Murphy, Lok Wong Samson, and Benjamin D Sommers. Covid-19 antivirals utilization: Geographic and demographic patterns of treatment in 2022. 2022.
- [3] Joseph Clayton, Vinícius Martins de Oliveira, Mohamed Fouad Ibrahim, Xinyuanyuan Sun, Paween Mahinthichaichan, Mingzhe Shen, Rolf Hilgenfeld, and Jana Shen. Integrative approach to dissect the drug resistance mechanism of the h172y mutation of sars-cov-2 main protease. *Journal of Chemical Information and Modeling*, 2023.
- [4] Kaifu Gao, Rui Wang, Jiahui Chen, Jetze J Tepe, Faqing Huang, and Guo-Wei Wei. Perspectives on sars-cov-2 main protease inhibitors. *Journal of medicinal chemistry*, 64(23):16922–16955, 2021.
- [5] Raimund Mannhold, Hugo Kubinyi, and Gerd Folkers. *Protein-ligand interactions*. John Wiley & Sons, 2012.
- [6] Douglas EV Pires, Tom L Blundell, and David B Ascher. mcsmlig: quantifying the effects of mutations on protein-small molecule affinity in genetic disease and emergence of drug resistance. *Scientific reports*, 6(1):29575, 2016.
- [7] Yanmei Hu, Eric M Lewandowski, Haozhou Tan, Xiaoming Zhang, Ryan T Morgan, Xiujun Zhang, Lian MC Jacobs, Shane G Butler, Maura V Gongora, John Choy, et al. Naturally occurring mutations of sars-cov-2 main protease confer drug resistance to nirmatrelvir. *ACS Central Science*, 9(8):1658–1669, 2023.
- [8] Stefan Elbe and Gemma Buckland-Merrett. Data, disease and diplomacy: Gisaïd’s innovative contribution to global health. *Global challenges*, 1(1):33–46, 2017.
- [9] Bronya J.B. Keats and Stephanie L. Sherman. Chapter 13 - population genetics. In David Rimoin, Reed Pyeritz, and Bruce Korf, editors, *Emery and Rimoin’s Principles and Practice of Medical Genetics (Sixth Edition)*, pages 1–12. Academic Press, Oxford, sixth edition edition, 2013. ISBN 978-0-12-383834-6. doi: <https://doi.org/10.1016/B978-0-12-383834-6.00015-X>. URL <https://www.sciencedirect.com/science/article/pii/B978012383834600015X>.
- [10] Douglas M Fowler and Stanley Fields. Deep mutational scanning: a new style of protein science. *Nature methods*, 11(8):801–807, 2014.
- [11] Tiqing Liu, Yuhmei Lin, Xin Wen, Robert N Jorissen, and Michael K Gilson. Bindingdb: a web-accessible database of experimentally determined protein–ligand binding affinities. *Nucleic acids research*, 35(suppl_1):D198–D201, 2007.

- [12] Stephen K Burley, Helen M Berman, Gerard J Kleywegt, John L Markley, Haruki Nakamura, and Sameer Velankar. Protein data bank (pdb): the single global macromolecular structure archive. *Protein crystallography: methods and protocols*, pages 627–641, 2017.
- [13] Renxiao Wang, Xueliang Fang, Yipin Lu, Chao-Yie Yang, and Shaomeng Wang. The pdbbind database: methodologies and updates. *Journal of medicinal chemistry*, 48(12):4111–4119, 2005.
- [14] Ashish Vaswani, Noam Shazeer, Niki Parmar, Jakob Uszkoreit, Llion Jones, Aidan N Gomez, Lukasz Kaiser, and Illia Polosukhin. Attention is all you need. *Advances in neural information processing systems*, 30, 2017.
- [15] Long Ouyang, Jeffrey Wu, Xu Jiang, Diogo Almeida, Carroll Wainwright, Pamela Mishkin, Chong Zhang, Sandhini Agarwal, Katarina Slama, Alex Ray, et al. Training language models to follow instructions with human feedback. *Advances in Neural Information Processing Systems*, 35:27730–27744, 2022.
- [16] Dong Chen, Kaifu Gao, Duc Duy Nguyen, Xin Chen, Yi Jiang, Guo-Wei Wei, and Feng Pan. Algebraic graph-assisted bidirectional transformers for molecular property prediction. *Nature communications*, 12(1):3521, 2021.
- [17] Pengyong Li, Jun Wang, Yixuan Qiao, Hao Chen, Yihuan Yu, Xiaojun Yao, Peng Gao, Guotong Xie, and Sen Song. An effective self-supervised framework for learning expressive molecular global representations to drug discovery. *Briefings in Bioinformatics*, 22(6):bbab109, 2021.
- [18] Rui Wang and Guo-Wei Wei. Persistent path laplacian. *Foundations of data science (Springfield, Mo.)*, 5(1):26, 2023.
- [19] Zixuan Cang, Lin Mu, and Guo-Wei Wei. Representability of algebraic topology for biomolecules in machine learning based scoring and virtual screening. *PLoS computational biology*, 14(1):e1005929, 2018.
- [20] Yao Zhao, Chao Fang, Qi Zhang, Ruxue Zhang, Xiangbo Zhao, Yinkai Duan, Haofeng Wang, Yan Zhu, Lu Feng, Jinyi Zhao, et al. Crystal structure of sars-cov-2 main protease in complex with protease inhibitor pf-07321332. *Protein & cell*, 13(9):689–693, 2022.
- [21] Changchuan Yin. Genotyping coronavirus SARS-CoV-2: methods and implications. *Genomics*, 112(5):3588–3596, 2020.
- [22] Rui Wang, Yuta Hozumi, Changchuan Yin, and Guo-Wei Wei. Decoding sars-cov-2 transmission and evolution and ramifications for covid-19 diagnosis, vaccine, and medicine. *Journal of chemical information and modeling*, 60(12):5853–5865, 2020.
- [23] Zhihai Liu, Yan Li, Li Han, Jie Li, Jie Liu, Zhixiong Zhao, Wei Nie, Yuchen Liu, and Renxiao Wang. Pdb-wide collection of binding data: current status of the pdbbind database. *Bioinformatics*, 31(3):405–412, 2015.

- [24] Tiejun Cheng, Xun Li, Yan Li, Zhihai Liu, and Renxiao Wang. Comparative assessment of scoring functions on a diverse test set. *Journal of chemical information and modeling*, 49(4): 1079–1093, 2009.
- [25] Yan Li, Li Han, Zhihai Liu, and Renxiao Wang. Comparative assessment of scoring functions on an updated benchmark: 2. evaluation methods and general results. *Journal of chemical information and modeling*, 54(6):1717–1736, 2014.
- [26] Minyi Su, Qifan Yang, Yu Du, Guoqin Feng, Zhihai Liu, Yan Li, and Renxiao Wang. Comparative assessment of scoring functions: the casf-2016 update. *Journal of chemical information and modeling*, 59(2):895–913, 2018.
- [27] Timothy J Trull and Ulrich W Ebner-Priemer. Using experience sampling methods/ecological momentary assessment (esm/ema) in clinical assessment and clinical research: introduction to the special section. 2009.
- [28] Dong Chen, Jiaxin Zheng, Guo-Wei Wei, and Feng Pan. Extracting predictive representations from hundreds of millions of molecules. *The journal of physical chemistry letters*, 12(44): 10793–10801, 2021.
- [29] Marta M Stepniewska-Dziubinska, Piotr Zielenkiewicz, and Pawel Siedlecki. Development and evaluation of a deep learning model for protein–ligand binding affinity prediction. *Bioinformatics*, 34(21):3666–3674, 2018.
- [30] Fergus Boyles, Charlotte M Deane, and Garrett M Morris. Learning from the ligand: using ligand-based features to improve binding affinity prediction. *Bioinformatics*, 36(3):758–764, 2020.
- [31] Dmitry S Karlov, Sergey Sosnin, Maxim V Fedorov, and Petr Popov. graphdelta: Mpn scoring function for the affinity prediction of protein–ligand complexes. *ACS omega*, 5(10): 5150–5159, 2020.
- [32] Norberto Sánchez-Cruz, José L Medina-Franco, Jordi Mestres, and Xavier Barril. Extended connectivity interaction features: improving binding affinity prediction through chemical description. *Bioinformatics*, 37(10):1376–1382, 2021.
- [33] Zechen Wang, Liangzhen Zheng, Yang Liu, Yuanyuan Qu, Yong-Qiang Li, Mingwen Zhao, Yuguang Mu, and Weifeng Li. Onionnet-2: a convolutional neural network model for predicting protein-ligand binding affinity based on residue-atom contacting shells. *Frontiers in chemistry*, 9:753002, 2021.
- [34] Mohammad A Rezaei, Yanjun Li, Dapeng Wu, Xiaolin Li, and Chenglong Li. Deep learning in drug design: protein-ligand binding affinity prediction. *IEEE/ACM Transactions on Computational Biology and Bioinformatics*, 19(1):407–417, 2020.
- [35] Shudong Wang, Dayan Liu, Mao Ding, Zhenzhen Du, Yue Zhong, Tao Song, Jinfu Zhu, and Renteng Zhao. Se-onionnet: a convolution neural network for protein–ligand binding affinity prediction. *Frontiers in Genetics*, 11:607824, 2021.

- [36] Derek Jones, Hyojin Kim, Xiaohua Zhang, Adam Zemla, Garrett Stevenson, WF Drew Bennett, Daniel Kirshner, Sergio E Wong, Felice C Lightstone, and Jonathan E Allen. Improved protein–ligand binding affinity prediction with structure-based deep fusion inference. *Journal of chemical information and modeling*, 61(4):1583–1592, 2021.
- [37] Duc Duy Nguyen, Kaifu Gao, Jiahui Chen, Rui Wang, and Guo-Wei Wei. Unveiling the molecular mechanism of sars-cov-2 main protease inhibition from 137 crystal structures using algebraic topology and deep learning. *Chemical science*, 11(44):12036–12046, 2020.
- [38] Ivan Gutman, Xueliang Li, and Jianbin Zhang. Graph energy. *Analysis of Complex Networks: From Biology to Linguistics*, pages 145–174, 2009.
- [39] Jason Z Xiang and B Honig. Jackal: A protein structure modeling package. *Columbia University and Howard Hughes Medical Institute, New York*, 2002.
- [40] G Madhavi Sastry, Matvey Adzhigirey, Tyler Day, Ramakrishna Annabhimoju, and Woody Sherman. Protein and ligand preparation: parameters, protocols, and influence on virtual screening enrichments. *Journal of computer-aided molecular design*, 27:221–234, 2013.
- [41] Fan Wu, Su Zhao, Bin Yu, Yan-Mei Chen, Wen Wang, Zhi-Gang Song, Yi Hu, Zhao-Wu Tao, Jun-Hua Tian, and Yuan-Yuan Pei. A new coronavirus associated with human respiratory disease in China. *Nature*, 579(7798):265–269, 2020.
- [42] Yuelong Shu and John McCauley. GISAID: Global initiative on sharing all influenza data—from vision to reality. *Eurosurveillance*, 22(13):30494, 2017.
- [43] Fabian Sievers and Desmond G Higgins. Clustal omega. *Current protocols in bioinformatics*, 48(1):3–13, 2014.
- [44] Dong Chen, Jian Liu, Jie Wu, Guo-Wei Wei, Feng Pan, and Shing-Tung Yau. Path topology in molecular and materials sciences. *The Journal of Physical Chemistry Letters*, 14(4):954–964, 2023.
- [45] Alexander A Grigor’yan, Yong Lin, Yu V Muranov, and Shing-Tung Yau. Path complexes and their homologies. *Journal of Mathematical Sciences*, 248:564–599, 2020.
- [46] Dong Chen, Jian Liu, Jie Wu, and Guo-Wei Wei. Persistent hyperdigraph homology and persistent hyperdigraph laplacians. *Foundations of Data Science*, 5:558–588, 2023.
- [47] Danijela Horak and Jürgen Jost. Spectra of combinatorial laplace operators on simplicial complexes. *Advances in Mathematics*, 244:303–336, 2013.
- [48] Beno Eckmann. Harmonische funktionen und randwertaufgaben in einem komplex. *Commentarii Mathematici Helvetici*, 17(1):240–255, 1944.
- [49] Rui Wang, Duc Duy Nguyen, and Guo-Wei Wei. Persistent spectral graph. *International journal for numerical methods in biomedical engineering*, 36(9):e3376, 2020.
- [50] Facundo Mémoli, Zhengchao Wan, and Yusu Wang. Persistent laplacians: Properties, algorithms and implications. *SIAM Journal on Mathematics of Data Science*, 4(2):858–884, 2022.

- [51] Afra Zomorodian and Gunnar Carlsson. Computing persistent homology. In *Proceedings of the twentieth annual symposium on Computational geometry*, pages 347–356, 2004.
- [52] Edelsbrunner, Letscher, and Zomorodian. Topological persistence and simplification. *Discrete & Computational Geometry*, 28:511–533, 2002.
- [53] Jian Liu, Jingyan Li, and Jie Wu. The algebraic stability for persistent laplacians. *arXiv preprint arXiv:2302.03902*, 2023.
- [54] Jacob Devlin Ming-Wei Chang Kenton and Lee Kristina Toutanova. Bert: Pre-training of deep bidirectional transformers for language understanding. In *Proceedings of naacL-HLT*, volume 1, page 2, 2019.
- [55] Kiersten M Ruff and Rohit V Pappu. Alphafold and implications for intrinsically disordered proteins. *Journal of Molecular Biology*, 433(20):167208, 2021.
- [56] Fabian Pedregosa, Gaël Varoquaux, Alexandre Gramfort, Vincent Michel, Bertrand Thirion, Olivier Grisel, Mathieu Blondel, Peter Prettenhofer, Ron Weiss, Vincent Dubourg, et al. Scikit-learn: Machine learning in python. *the Journal of machine Learning research*, 12:2825–2830, 2011.
- [57] Kaiming He, Xinlei Chen, Saining Xie, Yanghao Li, Piotr Dollár, and Ross Girshick. Masked autoencoders are scalable vision learners. In *Proceedings of the IEEE/CVF conference on computer vision and pattern recognition*, pages 16000–16009, 2022.
- [58] Dmitry Kozlov. *Combinatorial algebraic topology*, volume 21. Springer Science & Business Media, 2008.
- [59] László Lovász. Kneser’s conjecture, chromatic number, and homotopy. *Journal of Combinatorial Theory, Series A*, 25(3):319–324, 1978.
- [60] Franz Aurenhammer. Voronoi diagrams—a survey of a fundamental geometric data structure. *ACM Computing Surveys (CSUR)*, 23(3):345–405, 1991.
- [61] S Geršgorin. Bulletin de l’académie des sciences de l’urss. *Classe des sciences mathématiques et naturelles*, 6:749, 1931.
- [62] David Bramer and Guo-Wei Wei. Atom-specific persistent homology and its application to protein flexibility analysis. *Computational and mathematical biophysics*, 8(1):1–35, 2020.
- [63] Zixuan Cang and Guo-Wei Wei. Topologynet: Topology based deep convolutional and multi-task neural networks for biomolecular property predictions. *PLoS computational biology*, 13(7):e1005690, 2017.
- [64] Zixuan Cang and Guo-Wei Wei. Persistent cohomology for data with multicomponent heterogeneous information. *SIAM journal on mathematics of data science*, 2(2):396–418, 2020.
- [65] Xiaoqi Wei and Guo-Wei Wei. Persistent sheaf laplacians. *Foundations of Data Science (accepted)*. *arXiv preprint arXiv:2112.10906*, 2021.